MOX-Report No. 65/2024

Modeling Hypoxia Induced Radiation Resistance and the Impact of Radiation Sources

Possenti, L.; Vitullo, P.; Cicchetti, A.; Zunino, P.; Rancati, T.

MOX, Dipartimento di Matematica
Politecnico di Milano, Via Bonardi 9 - 20133 Milano (Italy)

mox-dmat@polimi.it https://mox.polimi.it

Modeling Hypoxia-Induced Radiation Resistance and the Impact of Radiation Sources

Luca Possenti[1]*, Piermario Vitullo[2]†, Alessandro Cicchetti[1], Paolo Zunino[2], Tiziana Rancati[1]

[1]Data Science Unit, Fondazione IRCCS Istituto Nazionale dei Tumori, Via Venezian 1, 20233 Milan, Italy

[2]MOX, Department of Mathematics, Politecnico di Milano, Piazza Leonardo da Vinci 32, 20233 Milan, Italy

Abstract

Hypoxia contributes significantly to resistance in radiotherapy. Our research rigorously examines the influence of microvascular morphology on radiotherapy outcome, specifically focusing on how microvasculature shapes hypoxia within the microenvironment and affects resistance to a standard treatment regimen ($30 \times 2Gy_{RBE}$). Our computational modeling extends to the effects of different radiation sources. For photons and protons, our analysis establishes a clear correlation between hypoxic volume distribution and treatment effectiveness, with vascular density and regularity playing a crucial role in treatment success. On the contrary, carbon ions exhibit distinct effectiveness, even in areas of intense hypoxia and poor vascularization. This finding points to the potential of carbon-based hadron therapy in overcoming hypoxia-induced resistance to RT. Considering that the spatial scale analyzed in this study is closely aligned with that of imaging data voxels, we also address the implications of these findings in a clinical context envisioning the possibility of detecting subvoxel hypoxia.

1 Introduction

Radiotherapy is a common treatment for cancer, used to treat more than half of patients [10]. Technological progress over the past three decades has greatly advanced radiation therapy. The high conformity to the cancer target together with the availability of various radiation sources are prime examples of this evolution [31]. Despite significant advances, cancer control continues to grapple with the complexities arising from both intratumor and intertumor heterogeneity. Central to these challenges is the interaction between oxygenation and radiation therapy, which also involves possible heterogeneity in tumor oxygenation.

Since the first observations in bacteria [1], hypoxia has been known to be a significant determinant of tumor resistance to RT, decreasing the damage induced by ionizing radiation [29]. Hypoxia, while generally defined as a shortage of oxygen, lacks a consistent quantitative measure. Severe hypoxia typically shows oxygen levels between 0.02% and 0.2% (0.15 to 1.5 mmHg), and moderate hypoxia up to 1% or 2% (7.6 or 15.2 mmHg). Furthermore, hypoxia is classified by cause: chronic hypoxia due to the distance from the oxygen-carrying vasculature to the tissue and acute hypoxia due to reduced blood flow that limits oxygen delivery.

Given the critical role of oxygen in RT, some imaging-based methods have been proposed to evaluate hypoxia in tissues, particularly tumors [29, 5, 30, 15]. Such methods take advantage of different technologies

*Corresponding Author

†The first two authors contributed equally to this work, sharing the first authorship

such as positron emission tomography (PET), near-infrared spectroscopy (but this is related to vascular oxygen) and magnetic resonance imaging (MRI), which allows the extraction of signals related to the oxygen content of the vascular compartments (BOLD signal) and the tissue compartments (TOLD signal) [9]. Using the TOLD method, hypoxic areas of the tumor were also correlated with the outcome of radiotherapy [81]. Further image-based methods have been proposed to identify hypoxic regions by signal combination. The method of Hompand et al. highlights hypoxic regions, estimating oxygen delivery from tissue consumption [28]. We must mention the resolution mismatch between the oxygen delivery scale, the imaging resolution, and the modulation of treatment [23]. In fact, oxygen delivery within the microenvironment occurs on a microscale (hundreds of μm), whereas voxels on the mm scale characterize the imaging [26], and treatment delivery is planned on a slightly larger scale. This scale mismatch motivates deeper analyzes involving different methods, from computational to *in vitro* and animal models [18].

The delivery of oxygen to microvessels is usually studied computationally by reducing the number of dimensions of the vascular system through various techniques. As a macroscopic approach, perfusion has been described using porous media [8, 40, 11]. Similarly, models that account for the local morphology of the microvasculature have been developed, for example, describing the microvasculature as a collection of concentrated sources; see, for example, [67] and more recently [73]. This seminal idea has evolved into more advanced multiphysics approaches [52, 37, 53], which encompass vascular and interstitial flow, red blood cell transport, oxygen transport, and allow mesoscale analysis of the vascular microenvironment. With this approach, Powathil et al. validated the prediction of their model against hypoxic markers and *in situ* oxygen measures [54]. To effectively simulate the intricate relationship between vascular networks and their environment, new strategies have been used to analyze blood flow and oxygen transfer [27], unraveling the impact of vascular transport and network morphology on tissue hypoxia in specific applications (e.g., brain [27, 19], tumor [54, 13]). Through a sensitivity analysis, we recently showed the effect of vascular density and morphology on oxygen distribution in tissue [77].

Few microvascular models have been applied to study radiation therapy and the microenvironment. Scott et al. described the interaction between vascular density and a morphological index [63]. In fact, they reported variations in the correlation between the morphological index and the outcome of treatment when considering different vascular densities. In a subsequent study, the same authors showed the importance of microvascular oxygen transport [24]. No evidence was found that microvascular morphology had any effect on the results of treatment, although oxygen variation in the vascular system was not considered. Schiavo et al. generated a vascular geometry cm-wide using a fractal approach with a hypovascularized core [62]. They studied chronic and acute hypoxia, showing how model parameters determine hypoxia, varying its position and area. In general, these studies suggest a key role for the vascular network in determining the outcome of RT.

When applying these models to RT, we must estimate the outcome of radiotherapy from computational oxygen distributions. To this end, the oxygen enhancement ratio (OER) shows the dose scale factor required to obtain the same tumor control when treating hypoxic versus normoxic tumors [12]. To consider radiation sources other than photons, we must evaluate the Relative Biological Effectiveness (RBE), which describes the dose ratio required to obtain the same damage with different radiation sources, testing a particular source, such as protons and carbon ions, against a reference one (usually photons)[12]. Hadrons have an RBE greater than 1, with a greater biological efficacy than photons. These radiations are also characterized by higher linear energy transfer (LET), the energy deposited per track length, measured by $keV/\mu m$. Interestingly, the OER is influenced by LET. For example, carbon ions typically have a higher LET than photons, and their effectiveness is less affected by the presence of hypoxia (that is, the OER is lower at a higher LET) [12]. Taking into account hypoxic imaging data, Garrido-Hernandez et al. compared treatment plans optimized using different models to account for RBE and OER [16]. They reported some differences in the prediction of the models, but even a significant effect of hypoxia.

Within this framework, our objective is to analyze the effect of microvasculature on radiation therapy using a state-of-the-art computational model. On the basis of these results, we address the influence of microvascular morphology (vascular density and regularity) on radiotherapy outcome to understand the role of the microvasculature. Furthermore, we show how this approach allows quantitative analysis of the

microvasculature and microenvironment in RT. Lastly, we extend this analysis to hadron therapy and altered oxygenation states to assess whether the role of microvasculature is consistent through different types of treatment and under other conditions.

2 Materials and methods

The workflow of this study comprises three steps: (i) generating different configurations of the geometry of the microvascular network, (ii) computing the oxygen concentration in the microvascular environment, and (iii) applying radiobiological models to estimate the result of radiotherapy. In the following paragraphs, we detail the methods for each step. The results are then analyzed and visualized by Paraview[36] and Prism[21].

2.1 Generation of microvascular networks

We consider a region of $1\,mm \times 1\,mm \times 150\mu m$ that describes an ideal portion of vascularized tissue. To generate representative vascular networks in that region, we adopt the previously proposed strategy [77]. This method uses Voronoi tessellation on a plane, resulting in a space-filling network following biomimetic principles [52, 70] and comprising bifurcation and anastomosis alone. As Voronoi networks are uniquely defined by a set of seed points, to initialize network generation, we adopt a two-step approach based on the placement of seed points in a square $1\,mm \times 1\,mm$, subdivided into *positive* and *negative* points, with opposite roles. First, we uniformly distribute a set of positive seeds in the plane. Then, a set of negative seeds is generated based on a Poisson distribution centered on $(0.5\,mm,\, 0.5\,mm)$. Each negative seed deletes a positive one, leading to a heterogeneous vessel distribution. Finally, a positive seed is added in the center of the square. Thanks to this method, we have produced networks characterized by different metrics. In particular, we control the surface-to-volume ratio S/V (the lateral surface of the network over the volume of the tissue) by controlling the positive seeds. In contrast, irregular morphology, quantified by the maximum distance of any point in the network (d_{max}), is determined by the ratio between the negative and positive seeds. Finally, we generate a quasi-3D network by moving the junctions and the boundary nodes along the direction perpendicular to the plane to fill the thickness of $150\,\mu m$.

We generate a set of 27 networks, representing 9 different conditions in triplicates (Figure S8). The nine conditions combine three values of S/V and three values of d_{max}, ranging from poor to highly vascularized tissues and from regular to irregular morphology (Table 1).

2.2 Modeling blood flow and oxygen transfer

The microvascular environment model used in this work belongs to the mesoscale approach family [68]. We describe the microenvironment as a three-dimensional domain, Ω, in which we embed the microvascular network represented as a collection of one-dimensional channels, i.e., the vascular domain is a metric graph denoted by Λ. In particular, coupling models at different dimensions requires specific mathematical methods [7, 38]. However, it brings some significant advantages at the computational level that will be discussed later.

In these two domains, we assembled three mathematical problems that describe different phenomena: (i) fluid flow $\mathcal{F}$ [7], (ii) transport of red blood cells $\mathcal{H}$ [52], (iii) transport of oxygen $\mathcal{O}$ [53].

2.2.1 Microvascular flow and red blood cells transport

First, we model fluid flow within the vasculature and surrounding tissue ($\mathcal{F}$). An interstitial fluid is described as a Newtonian fluid in a porous medium, employing Darcy's equation. On the other hand, we use the Poiseuille equation for blood flow in the vasculature. The effects of red blood cells ($\mathcal{H}$) are included in the model considering their effect on viscosity by the Fahraeus-Lindqvist effect [55], and their splitting when traveling in a bifurcation, that is, the Zweifach-Fung effect [64]. The classical Starling equation describes

fluid filtration through the microvascular wall, which accounts for hydraulic and osmotic pressures. The problem is complemented by the mass conservation equations in the two domains (tissue Ω and vasculature Λ), and it reads as follows:

$$\mathcal{F}+\mathcal{H}:\begin{cases} \boldsymbol{u}_t+\dfrac{\mathrm{K}}{\mu_t}\nabla p_t=0 & \text{in } \Omega \quad \text{(Darcy's eq.)} \\ \nabla\cdot\boldsymbol{u}_t-\phi_V\delta_\Lambda=0 & \text{in } \Omega \quad \text{(mass conservation eq.)} \\ 8\mu_v u_v+R^2\partial_s p_v=0 & \text{in } \Lambda \quad \text{(Poiseuille's eq.)} \\ \partial_s(\pi R^2 u_v)+\phi_V=0 & \text{in } \Lambda \quad \text{(mass conservation eq.)} \\ \phi_V=2\pi R L_p\big((p_v-\overline{p}_t)-\sigma(\pi_v-\pi_t)\big) & \text{in } \Lambda \quad \text{(Starling's eq.)} \\ \pi R^2 u_v\partial_s H-\phi_V H=0 & \text{in } \Lambda \quad \text{(RBCs transport eq.)} \end{cases} \tag{1}$$

where the subscripts t and v represent the tissue and vasculature, respectively, u is the fluid velocity, p is the fluid pressure, μ is the viscosity, K is the porous medium permeability, R is the radius of the vessel, ϕ_V fluid flow across the vascular wall affected by the vascular hydraulic conductivity, L_p, the reflection coefficient for proteins, σ and the osmotic pressure, π. Further details on modeling equations, procedures to handle network junctions, and numerical solutions to the problem can be found in [52, 50]. The problem is then defined by considering boundary conditions, setting variable values for the inlet and outlet pressures, and the hematocrit inlet. For tissue, homogeneous conditions are enforced so that no flow can leave the domain.

2.2.2 Oxygen transport

The oxygen transport equations ($\mathcal{O}$) for the two domains comprise diffusion, consumption, and advection, using data from the models $\mathcal{F}$ and $\mathcal{H}$ in a one-way coupling scenario. In addition to the component mentioned above, we introduce three phenomena: (i) oxygen binding to hemoglobin, (ii) oxygen uptake dynamics, and (iii) oxygen exchanges through microvascular walls.

For the first, we recall that oxygen is present in the system as solved in plasma/interstitial fluid (C_v or C_t) or bound to hemoglobin (C_{HbO_2}). The total oxygen content is the sum of the two in the vasculature, the region containing RBC and hemoglobin. We assume the binding dynamics as an instantaneous process, described by the Hill's equation:

$$C_{HbO_2}(C_v)=k_1\,H\,S(C_v)=k_1\,H\,\frac{C_v^{\gamma_{Hb}}}{C_v^{\gamma_{Hb}}+(\eta_{pl}\;p_{s_{50}})^{\gamma_{Hb}}} \tag{2}$$

where k_1 is a constant value determined by the product of the Hüfner factor (HF) describing the oxygen binding capacity of human hemoglobin and the Mean Corpuscular Hematocrit Concentration ($MCHC$). The remaining parameters of (2) are oxygen solubility in plasma η_{pl}, the oxygen partial pressure at half-saturation of hemoglobin $p_{s_{50}}$, and the Hill exponent γ_{Hb}.

Secondly, we describe the cell uptake in the tissue by the well-known Michaelis-Menten equation [46]:

$$R_t(C_t)=V_{max}\;\frac{C_t}{C_t+\eta_t\;p_{m_{50}}} \tag{3}$$

where V_{max} is the maximum oxygen consumption rate, η_t is the oxygen solubility in the tissue, and $p_{m_{50}}$ is the Michaelis-Menten constant, i.e. the oxygen partial pressure at half consumption rate.

The oxygen exchanges include diffusion and advection through the microvascular wall as a semi-permeable membrane [33]:

$$\phi_{O_2}=2\pi R\;P_{O_2}(C_v-\boldsymbol{ct})+\left(\frac{C_v+\boldsymbol{ct}}{2}\right)\;\phi_V \tag{4}$$

where P_{O_2} is the microvascular wall permeability.

Comprehensively, the oxygen transport model reads as follows:

$$\mathcal{O}: \begin{cases} \nabla \cdot (-\varepsilon_t \nabla C_t + \mathbf{u}_t\ C_t) + R_t(C_t) = \phi_{O_2}\, \delta_\Lambda & \text{on } \Omega \\ \pi R^2 \dfrac{\partial}{\partial s}\left(-\varepsilon_v \dfrac{\partial C_v}{\partial s} + u_v\big(C_v + C_{HbO_2}(C_v)\big)\right) = -\phi_{O_2} & \text{on } \Lambda \end{cases} \tag{5}$$

where $\varepsilon_*, * = v, t$ are the diffusion coefficients in the blood and tissue compartments. The model describes oxygen transport through the microvasculature and delivery to tissue through flux ϕ_{O_2}. This mixed-dimensional mathematical formulation combines a 3D region Ω, with a 1D network Λ. At the mathematical level, the coupling between the two is provided by a Dirac measure distributed throughout the network, denoted by δ_Λ. Eventually, oxygen reaches the cells and cell uptake occurs. The problem is complemented by boundary conditions that define oxygen concentrations at network inlets, the null derivative at network outlets, and null concentration gradients at the tissue faces, i.e., no diffusive flux. Complete details related to the derivation, discretization, solving, and validation of the model are reported in [53].

2.3 Simulations of oxygen transport in the microenvironment

For complex geometrical configurations, explicit solutions to the problems $\mathcal{F}$, $\mathcal{H}$, $\mathcal{O}$ are not available. Numerical simulations are the only way to apply the model to real cases. The discretization of these models, described in [52], is achieved by the finite element method (Appendix A). Due to the peculiar mathematical structure of the model, based on mixed-dimensional differential equations, no commercially available simulator can handle it. All simulations have been performed using an internal C++ code based on the GetFem++ open-source library [57].

The main advantage of the mixed-dimensional formulation adopted here is that the discretizations of the equations defined in the tissue and the vascular network are entirely independent with respect to the computational grids and the numerical schemes. We discretize the branches of the vascular network as separate subdomains. A piecewise straight line approximates each of them. The problems of blood flow and oxygen transfer are approximated using continuous piecewise polynomial finite elements. The interstitial flow problem is approximated by using mixed finite elements.

Because of the non-linear relationships present in the constitutive laws of the model, the problem has been linearized, and the solution of the coupled problem has been reached via an iterative process. At each iteration, the numerical discretization schemes described above provide a high-dimensional linear system of equations solved employing state-of-the-art iterative (linear) solvers with suitable preconditioners. We refer to [52, 6, 7, 38] for further details on computational methods.

The ideal tissue slab with dimension $1\,mm \times 1\,mm \times 150\mu m$ has been discretized through a uniform tetrahedral mesh of $40 \times 40 \times 6$ nodes on each side, consisting of 57600 tetrahedra. This numerical resolution has been considered satisfactory after performing a mesh sensitivity analysis. In particular, the mean relative error in the L^2 norm on the approximation of the oxygen partial pressure between the considered mesh and a new one with higher resolution (precisely $50 \times 50 \times 8$ points per side) resulted in less than 3%.

The simulation of each blood flow and oxygen transfer scenario discussed below is not computationally demanding on a multi-core processor with good performance. Scaling up these computations to the tumor scale will require high-performance computing platforms.

2.4 Radiobiological models for the radiotherapy outcome

We model radiotherapy treatment using the linear-quadratic model (LQ), the most widely used radiological model. It is based on two different parameters that describe the radiosensitivity of cells or tissue. The first parameter α describes the lethal damage resulting from a 'single' hit, whereas β is related to 'multiple' hits, namely the interaction of multiple radiation tracks [45]. Combining these two parameters and the dose administered (D), the surviving fraction (SF) is estimated as follows:

$$SF(D) = e^{-\alpha D\ -\beta D^2}. \tag{6}$$

The values of SF range from 0 to 1, representing the fraction of cells that survived treatment with the specified dose D. In current clinical practice, the total dose is divided into fractions n_f, usually administered daily, that is, fractionated treatments [10]. A slightly modified LQ model describes the cumulative effect of each fraction by recursive application of the model:

$$SF(D) = \prod_{n_f} \left(e^{-\alpha d \ -\beta d^2} \right) \ = \ e^{n_f \left(-\alpha d \ -\beta d^2 \right)} \tag{7}$$

where $d = D/n_f$ is the fraction dose. We remark that tumor growth during treatment is not included in this equation.

Due to the small tissue region analyzed, we assume a constant dose D on the volume. The same assumption is invalid for oxygen content, which may differ throughout the region, affecting treatment results. To account for the oxygen effect, we adopt two different models: the Wenzl model (WEN) [79, 80] and the Tinganelli model (TIN) [74]. These are modifications of the classical LQ model. The model proposed by Wenzl and colleagues defines the variation of α and β with the oxygen partial pressure and the linear energy transfer (LET) of ionizing radiation:

$$\begin{aligned} \alpha(\boldsymbol{x}, pO_2, LET) \ &= \frac{(a_1 \ + a_2 \ LET) \ pO_2(\boldsymbol{x}) \ + \ (a_3 \ + a_4 \ LET) \ k_{RT}}{pO_2(\boldsymbol{x}) + \ k_{RT}} \\ \sqrt{\beta(\boldsymbol{x}, pO_2)} \ &= \frac{b_1 \ pO_2(\boldsymbol{x}) + \ b_2 \ k_{RT}}{pO_2(\boldsymbol{x}) + \ k_{RT}} \end{aligned} \tag{8}$$

where k_{RT} is the oxygen tension for radiosensitivity equal to half of its maximum value. Expressions of $\alpha(\boldsymbol{x}, pO_2, LET)$ and $\beta(\boldsymbol{x}, pO_2)$ are inserted directly into the LQ equation:

$$SF(D) = e^{n_f \left(-\alpha(\boldsymbol{x}, pO_2, LET) d \ -\beta(\boldsymbol{x}, pO_2) d^2 \right)}. \tag{9}$$

On the contrary, the Tinganelli model is based on the definition of the Oxygen Enhancement Ratio (OER), which is then used to scale the dose:

$$\begin{aligned} OER(0, LET) \ &= \frac{LET^{\gamma} + M \ a}{a + LET^{\gamma}} \\ OER(\boldsymbol{x}, pO_2, LET) \ &= \frac{b \ OER(0, LET) + pO_2(\boldsymbol{x})}{b + pO_2(\boldsymbol{x})} \\ D_{OER}(\boldsymbol{x}, pO_2, LET) \ &= \frac{D}{OER(pO_2(\boldsymbol{x}), LET)} \end{aligned} \tag{10}$$

where M, a, γ, b are parameters fitted to experimental data, and $D_{OER}(\boldsymbol{x}, pO_2, LET)$ is the dose corrected for the oxygen effect, to be included in the LQ model. Therefore, the TIN values α and β do not change with LET or pO_2, and the resulting model reads as follows:

$$SF(D) = e^{n_f \left(-\alpha \frac{d}{OER(pO_2(\boldsymbol{x}), LET)} \ -\beta \left(\frac{d}{OER(pO_2(\boldsymbol{x}), LET)} \right)^2 \right)}. \tag{11}$$

To properly compare the models, we used the parameters of the WEN model published in [79], and fit the TIN parameters to the data reported by WEN and colleagues. Further details on the parameter and the fitting procedure are described in the Appendix A.

These two LQ-based models allow us to compute the $SF(\boldsymbol{x})$. Based on that, we calculate the tumor control probability (TCP), which describes the probability of successful treatment. It is based on the number of cells surviving the treatment (SF) and the initial number of clonogenic cells N:

$$TCP(D) = e^{-N \cdot SF(D)}. \tag{12}$$

In particular, since we analyze the spatial variability of the radiotherapy response on the microscale, we describe SF as a spatially dependent map $SF(D, \boldsymbol{x})$. We employ the methods presented in [71] to compute

the $TCP(D)$ from the SF distribution, leveraging the Poisson process assumption and the 'parallel-like' behavior of the tumor (i.e., even a small portion of the tumor surviving results in tumor relapse, and therefore TCP is low):

$$TCP(D) = \prod_i TCP(D, \boldsymbol{x_i}) = \prod_i e^{-N_i \ SF(D, \boldsymbol{x_i})}. \tag{13}$$

In summary, we obtain $pO_2(\boldsymbol{x})$ in the tissue that solves $\mathcal{F}$, $\mathcal{H}$, and $\mathcal{O}$. We compute $SF(\boldsymbol{x})$ applying the WEN and TIN models. Finally, we consider the spatial distribution $SF(\boldsymbol{x})$ to obtain a probability value for $TCP(D)$ (equation 13).

2.5 Simulated treatment schedule and sources

We initially define the treatment schedule for photons, the most common radiation therapy treatment. The total treatment dose is 60 Gy, divided into 30 fractions at 2 Gy per fraction, that is, a treatment $30 \times 2Gy$. We point out that this treatment is compatible with the clinical schedules and the clinical dose received by the tumors. For example, non-small cell lung cancers receive $30 \times 2Gy$ [56], and prostate cancer patients are usually treated with $60 - 72$ Gy in fractions $20 - 30$ [82]. In our setting, $30 \times 2Gy$ treatment guarantees a highly successful treatment ($TCP \simeq 1$) in well-oxygenated tumors ($pO_2 > 5$ $mmHg$).

Furthermore, we analyze a similar treatment schedule for hadron therapy, particularly for protons and carbon ions. These different sources have different biological effects. To consider this, the dose is usually scaled by RBE [12]. Consequently, two different doses are defined: the physical dose, that is, the actual dose physically measured, and the biological dose scaled by RBE. The biological dose is then used in the LQ models. We compare different sources considering the same biological dose (2 Gy_{RBE} per fraction); the physical dose is $2/RBE$ Gy per fraction. Photons and hadrons also differ in LET (photons: 2 $keV/\mu m$; protons: 4 $keV/\mu m$; carbon ions: 75 $keV/\mu m$ [12, 35]), which enters the radiobiological models and determines the response to hypoxia.

2.6 Oxygenation scenarios

We evaluated the level of oxygenation pO_2 in the microenvironment, within the domain Ω under three different scenarios. The baseline scenario represents a typical tumor tissue without specific characteristics (see Table 1). The second scenario simulates reduced oxygen delivery due to decreased blood flow, a condition known as acute hypoxia (AH) [75, 29]. The third scenario involves a higher level of oxygen consumption by the tumor, which exacerbates any chronic hypoxia from the baseline. This type of hypoxia, related to diffusion limitations, depends on the distance from the nearest blood vessel [75, 29]. Elevated oxygen consumption effectively shortens the diffusion distance prior to cellular uptake.

3 Results

We quantify the outcome of radiotherapy (i.e., tumor control) by referring to different sources (photons, protons, and carbon ions) and various states of oxygenation in the microenvironment. For each case, we solve fluid dynamics $\mathcal{F}$, red blood cell transport $\mathcal{H}$, and oxygen delivery $\mathcal{O}$. The oxygen distribution is then used to estimate the surviving fraction (SF) and the corresponding tumor control probability (TCP) using two different formulations of the Linear Quadratic model modified for the oxygen content. The results are presented starting from the classical photon-based RT. The effects of hadron therapy are studied, as well as the implications of non-standard oxygenation levels.

3.1 Variations in oxygen distribution due to microvascular density and morphology

The microvascular density and morphology generally affect the oxygen distribution in the microenvironment. When considering a regular network, tissue oxygenation increases with microvascular density, as evidenced

by the first row of the panel 1-a, and quantified by graph 1-b (blue columns referring to the lower d_{max}). The same trend is also reported for irregular networks for higher d_{max} values. In contrast, increasing d_{max} effectively reduces the average partial oxygen pressure in medium and highly vascularized cases only. In the low-vascularized case, the regularity of the network has little to no effect. The resulting oxygen content is consistent with the ranges described in the literature, which differ between tissues due to differences in vascularization and tissue oxygen demand [5, 58, 4].

Microvascular density and morphology generally determine the hypoxic volume fraction. The more irregular the network, the larger the low oxygen fraction (Figs. 1, cf. and S9). Additionally, a denser microvascularization results in smaller low-oxygen fractions.

High vascularization does not guarantee the absence of hypoxic regions, as indicated by hypoxic volume in case $S/V = 14mm^{-1}$, $d_{max} = 240\mu m$. Generally, a higher degree of irregularity (d_{max}) is required to produce hypoxia in higher vascularized tissues. For example, the hypoxic volume appears in the case $S/V = 7mm^{-1}$, $d_{max} = 160\mu m$, but not in $S/V = 14mm^{-1}$, $d_{max} = 160\mu m$.

3.2 Computing TCP with photons RT

We computed the surviving fraction $SF(\boldsymbol{x})$ and the corresponding tumor control probability using the two radiobiological models (Wenzl model - WEN [79, 80] and the Tinganelli model – TIN [74]; Fig. 2). Good vascularization with regular microvascular morphology determines a tiny or null hypoxic fraction (Fig. 1 c-f), and therefore a TCP $\rightarrow$ 1, that is, a successful treatment ($S/V = 7mm^{-1}$ - $d_{max} = 120\mu m$, and $S/V = 14mm^{-1}$ - $d_{max} = \{120; 160\}\mu m$). Even a tiny hypoxic volume (considering the strong definition with $pO_2 \leq 1\ mmHg$) produces an evident drop in TCP, as can be seen in cases $S/V = 7mm^{-1}$ - $d_{max} = 160\mu m$. The highly irregular morphology of the network reduces TCP under all conditions, as shown by the drop in TCP when considering cases $S/V = 14\ mm^{-1}$.

Data show that increased vascularization generally improves TCP, while morphological irregularities have a detrimental effect on the outcome of the treatment. This is especially evident with the TIN model, which is characterized by a less sharp response to hypoxia.

An irregular microvascular morphology can determine a poor treatment outcome, even in highly vascularized tissues. A similar result can be achieved with a regular low-density microvascular network. In fact, the TCPs for cases $S/V = 14mm^{-1}$ - $d_{max} = 240\mu m$ and $S/V = 3.5mm^{-1}$ - $d_{max} = 120\mu m$ are similar.

3.3 Comparing TCP from photons and hadron therapy

We analyze the cases treated with protons and carbon ions using the same biological dose and schedule (Fig. 3). First, proton-based radiotherapy has outcomes similar to those of photon treatment. Therefore, considerations of microvascular architecture and morphology still hold for proton therapy, determining the outcome of the treatment. Again, increased vascularization and morphological regularity improve TCP. As a result, carbon ions effectively treat all cases analyzed without the influence of microvascular density and morphology. We remark that we are using the same biological dose, and consequently, a similar outcome is expected. However, they differ slightly for protons and more evidently for carbon ions. This is due to the different LET associated with the two sources: 2 $keV/\mu m$ for photons, 4 $keV/\mu m$ for protons, and $LET = 75\ keV/\mu m$) [12, 35]. LET determines also the response to hypoxia, as can be seen in equations 8 and 10. In particular, ionizing radiation characterized by greater LET results in being less sensitive to hypoxia-mediated radioresistance. Therefore, they result in a higher TCP. This effect is slightly noticeable when comparing photons and protons, but is evident when considering carbon ions.

3.4 Influence of acute hypoxia and tumor oxygen consumption

We tested the same vascular conditions, reducing the vascular flow rate and increasing tumor oxygen demand, keeping all other parameters at their reference values. Among the two, increased consumption induces a more potent reduction in oxygenation within the tissue (Fig. 4), in agreement with previous work on oxygenation [53, 66, 65]. An essential difference between the two scenarios is how they act in the two domains. Acute

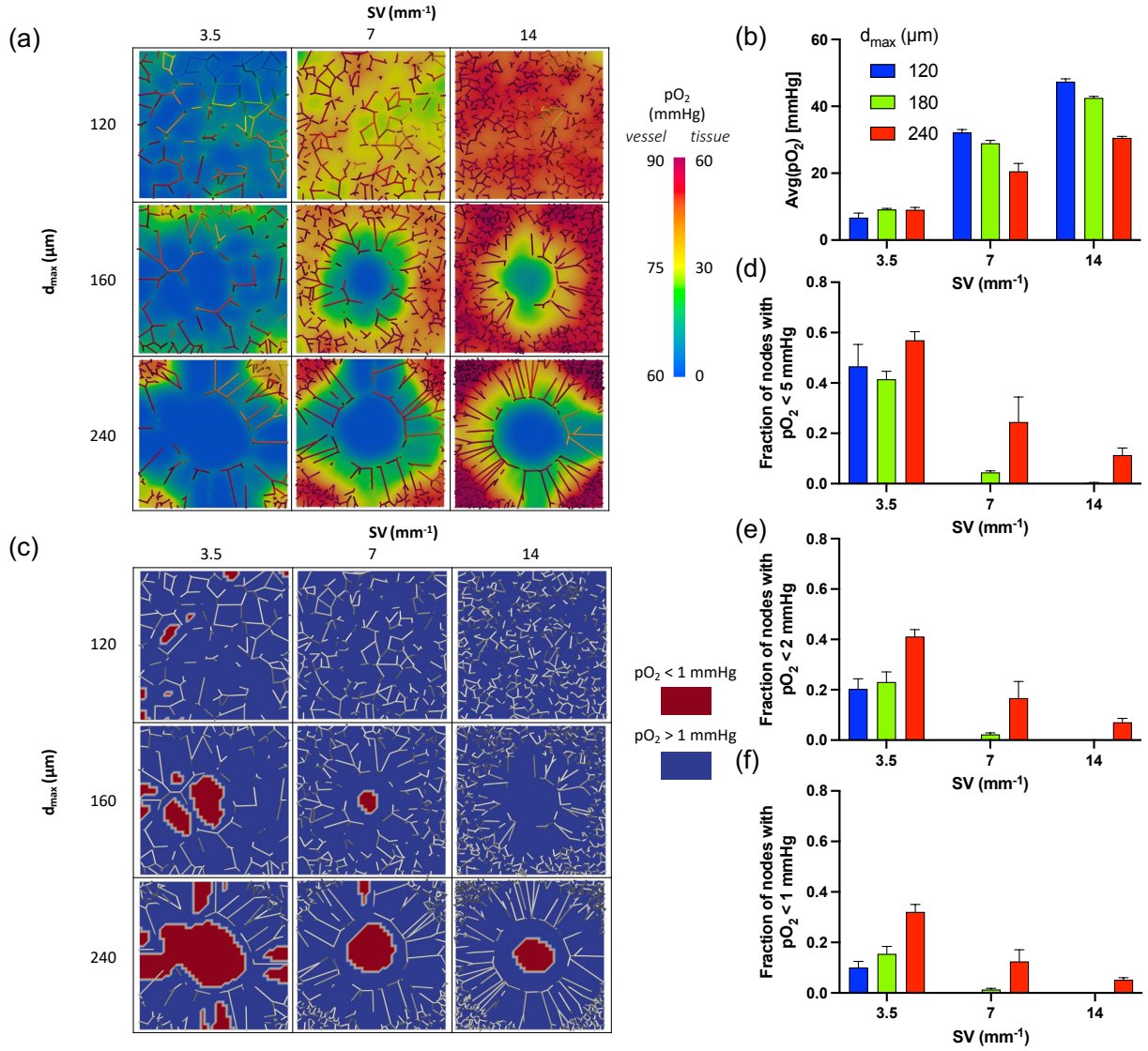

Figure 1: **Oxygen distribution in the nine cases for the reference scenario.** (a) Oxygen partial pressure in the tissue Ω and microvascular Λ domains. A single replicate of the nine cases (3 $S/V \times 3$ d_{max}) is shown. (b) Average oxygen partial pressure in the tissue in the nine cases considered. (c) Localization of low oxygen areas, setting a threshold (th) equal to 1 $mmHg$. Similar maps for $th = 2mmHg$ and $th = 5mmHg$ are available in the figure S9. The other panels show the fraction of nodes below the threshold in the nine cases, setting the threshold to 5 $mmHg$ (d), 2 $mmHg$ (e), and 1 $mmHg$ (f).

hypoxia first acts on the microvascular network, leading to a more pronounced decrease of pO_2 in the network (Fig. 4a compared to the left columns). On the other hand, an increase in consumption reduces the oxygen concentration of the tissue uniformly, with lower effects on the network. Higher oxygen consumption increases the microvascular density required to ensure good oxygenation. The levels in the average partial oxygen pressure for the cases $d_{max} = \{120,\ 160,\ 240\}\mu m$ - $S/V = 7mm^{-1}$ - *High consumption* are similar to those of $d_{max} = \{120,\ 160,\ 240\}\mu m$ - $S/V = 3.5mm^{-1}$ - *Reference*, showing an insufficient microvascular density.

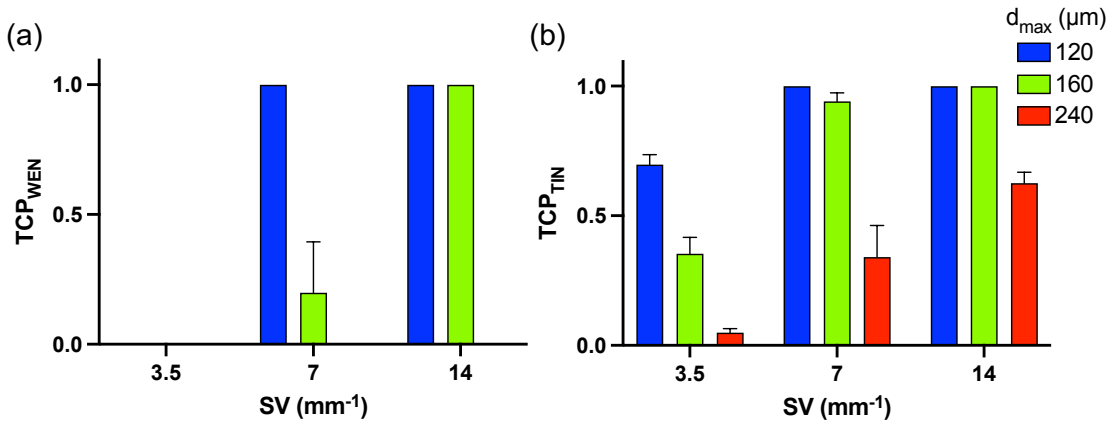

Figure 2: **Computed TCPs for the nine cases with photons RT.** Resulting TCPs referred to $30 \times 2Gy$ treatment with photons radiotherapy using the WEN (a) and the TIN (b) models applied to the 9 cases ($3\ S/V \times 3\ d_{max}$). TCP $\rightarrow$ 1 depicts successful treatments.

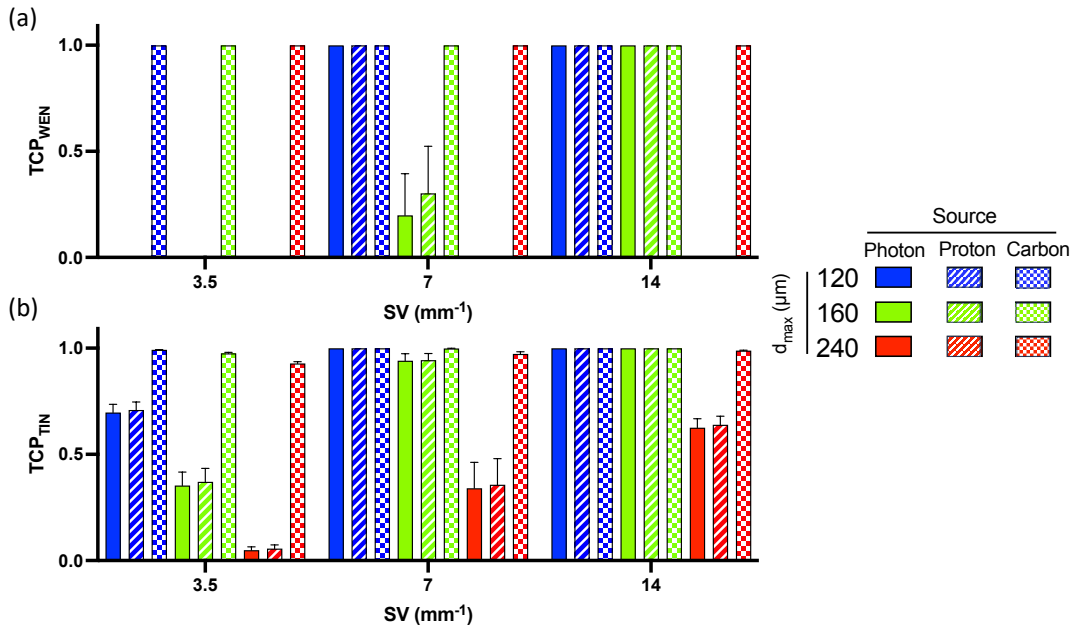

Figure 3: **Computed TCPs for the nine cases with three different sources: photons, protons, and carbon ions.** Resulting TCPs referred to $30 \times 2Gy_{RBE}$ treatment using the WEN (a) and the TIN (b) models. radiotherapy treatment is simulated considering photons, protons, and carbon ions applied to the 9 cases ($3\ S/V \times 3\ d_{max}$). TCP $\rightarrow$ 1 depicts successful treatments.

Increased oxygen consumption creates larger hypoxic volumes with $pO_2 \leq 1\ mmHg$, with a wide impact on different microvascular conditions (Fig. 5). We note that the hypoxic volume fraction generally decreases with vascular density and increases in perturbed vascular scenarios. Hypoxia is also significantly present in the highly vascularized scenario if the morphology is irregular.

Finally, the alterations observed in hypoxic volumes at low vascular density report a peculiar pattern. For acute hypoxia and high consumption rates, the transition from regular to perturbed vascular morphology

leaves the volume fraction of hypoxic tissue almost unchanged. In these scenarios, vascular renormalization would not improve tissue oxygenation. In fact, regular networks are more affected than irregular networks by acute hypoxia and high consumption. This different behavior in low-vascularized tissues agrees with data previously shown with a 2d-0d model [63].

3.5 Comparing TCP in different scenarios

Using oxygen distributions, we estimate TCPs under different oxygenation scenarios considering three treatments (Fig. 6a-b). A lower microvascular density and a considerably irregular morphology (that is, a high d_{max}) decrease the probability of a successful treatment with photons and protons. Furthermore, mid-microvasularization with mid-regularity results in better TCP (although often unsuccessful) than irregularly highly vascularized and regular low-vascularized cases. However, carbon treatment has high TCPs in all cases considered, showing a very low dependence on microvascular characteristics.

We compare the correlations among the oxygen data and the resulting TCPs when considering photons (Fig. 6c-d). The average pO_2-TCP plot shows a "safe area" depicting successful treatments ($TCP \to 1$) for an average oxygen partial pressure greater than 32 $mmHg$, ensuring a treatment without oxygen-related radioresistance problems. Below this threshold, the TCP is more scattered, showing that this index is not a good marker of treatment failure. On the other hand, the hypoxic volume fraction ($pO_2 < 1$) is strictly correlated with the outcome of the treatment ($R^2 = .73,\ p < .0001$). As also shown in the previous results, proton treatments lead to similar results when analyzing the hypoxia-TCP correlation (Fig. 6e). Carbon still shows a correlation, but with a lower influence of hypoxia (coefficient of linear regression $log_{10}TCP$ - hypoxic volume fraction: photons -1.669; protons -1.673; carbon -0.247).

We note that the correlation of hypoxia with radioresistance is not surprising (see Section 2.4). These results highlight the contribution to hypoxia at the microvascular scale, which shows the role of microvascular morphology.

With the exclusion of carbons, favorable microvascular networks determine the success of treatment, that is, high TCP. To unravel the role of the microvascular network, we define the vascular index as the sum of two scores for the density of vascularization (1 = high, 2 = medium, 3 = low) and the morphology (1 = regular, 2 = medium, 3 = irregular). Therefore, the lowest vascular score (= 2) represents a highly vascularized regular network. Then, the vascular score of 3 comprises a medium-vascularized regular network and a highly vascularized network with medium irregularities. The TCP is close to one if the vascular index is lower than four. Indeed, the TCP starts to drop monotonically at this level with increasing index. Interestingly, the vascular index equal to four includes heterogeneous conditions between the two indices (high-density irregular or low-density regular), which shows the importance of a comprehensive characterization of the microvascular network in terms of density and morphology.

4 Discussion

The concept of Biological Target Volume (BTV) brings radiobiological characteristics to radiation treatment. In this framework, tumor oxygenation represents essential information that can be collected through imaging. PET scans demonstrate the existence of hypoxic areas within tumors, and hypoxia has been shown to be an accurate predictor of the results of radiation treatment. However, translation of this information into a biologically optimized treatment plan through dose painting has not reached clinical practice [76, 61]. The dynamic nature of hypoxia is believed to be one of the reasons for limiting dose-painting techniques, also considering that changes in hypoxic volume are predictive of local recurrence [39]. Another problem lies in the so-called resolution gap. In fact, the voxels of the imaging data are typically on the millimeter scale, whereas oxygen diffusion occurs on the micrometer scale [23]. Consequently, different oxygen distributions can have similar PET signals that mask the intra-voxel heterogeneity.

In this framework, computational models can be used to study the state of oxygenation at the microscale, as proposed in [22]. We analyze by computational models the effect of microvascular morphology on oxygenation and, eventually, on the outcome of radiation therapy. Some evidence in the literature particularly

motivates the use of computational models to analyze different oxygenation scenarios. Grogan et al. conducted a similar study showing how 2D and 3D representations differ when analyzing microvascular oxygen delivery and reported a negligible influence of microvascular morphology on tissue oxygenation [24]. Scott and coworkers reported a non-trivial influence of the microvasculature on radiotherapy. More in detail, the morphology of the network is differently correlated with the outcome of therapy when considering high and low vascular density [63]. Schiavo et al. simulated an idealized tumor vasculature with heterogeneous vascular density and morphology with low vascularization toward the center of the tumor [62]. Various factors associated with microvascular conditions have been shown to have an effect on the oxygenation and radiation results of a tumor that is one centimeter wide in scenarios that are clinically applicable and involve diffusion and perfusion limited hypoxia.

These research works primarily examine how oxygen diffuses within tissues. More comprehensive models that incorporate blood flow and red blood cells within the microvascular network offer a more detailed understanding[53, 64, 20, 14]. This approach helps explain the uneven distribution of oxygen in vessels and its impact on oxygen delivery, altering how the microvascular structure affects the outcomes of radiation therapy. Our study is based on a microscale oxygenation model that describes both vascular and tissue [53], applied to a domain comparable to a single imaging voxel (millimeter scale), obtaining tissue oxygen levels consistent with the literature [5, 58]. In our scenarios, we reproduced different levels of hypoxia down to a few $mmHg$ (as reported by Muz et al. [49]), and we simulated treatments with clinically relevant schedules.

We report a strong correlation between TCP and hypoxic volume ($pO_2 \leq 1\, mmHg$, Figure 6). Anyway, such a correlation originates from the oxygen distribution at the microscale, reaching a subvoxel resolution. In contrast, it is lost when the resolution is limited to the size of the voxel, namely by limiting the oxygen knowledge to a single value (Figure 6). This confirms the presence of the resolution gap described by Grimes et al. [23]. Using the mean pO_2 as a representative value, we can only identify a threshold required to obtain a successful treatment ($pO_2|_{avg} \geq 32\, mmHg$), but the outcome of treatment is highly scattered in the case of lower oxygenation.

In terms of clinical translation, these data suggest that any local de-escalation in dose painting must be approached with caution, given the current imaging capabilities. Due to resolution limitations, information available at the voxel level can hide local hypoxic spots. These areas could significantly reduce TCP, even to 10^{-1} when the average pO_2 ranges from 10-20 mmHg.

Our results show the effect of microvasculature on radiotherapy (Figures 3,6). A significant decrease in TCP is independent of low vascular density or highly disordered morphology. We note that different vascular geometries can represent various tumors but also different regions within the same tumor, as shown in [62]. Furthermore, the combination of vascular density, shape, flow, and oxygen consumption can produce complex results in terms of the average oxygenation within the voxel (Figures 1, 4). In contrast, we do not report similar effects in the hypoxic regions ($pO_2 \leq 1\, mmHg$) and, consequently, in TCP. These results differ from those reported by Scott et al. [63]. However, a direct comparison is difficult due to the different metrics, model dimensionality, and modeled cell phenomena (e.g., cell proliferation).

In addition to classical photon-based radiation therapy, we also considered hadron therapy, which represents an alternative treatment to overcome tumor hypoxia. A higher LET is associated with a lower OER with less pronounced oxygen-mediated radio-resistance [12, 79]. In our study, we considered protons ($LET = 4\ keV/\mu m$) and carbon ions ($LET = 75\ keV/\mu m$). Consistently, the proton results are similar to those of the photon ones, whereas the carbon ions deviate toward better control of the tumor in all cases, namely, controlling hypoxic tumors. Such results are consistent with a similar study, in which carbon ion fractionated radiotherapy successfully controls hypoxic tumors [2]. When considering the results, we can identify cases that benefit from carbon-ion treatment. Our simulations show a clear benefit when the vascular index is greater than 4, highlighting the role of the microvasculature.

Dose escalation represents another alternative to address hypoxia-related tumor radioresistance. This work presents a computational model that enables us to assess the impact of the shape of the microvascular network in a dose escalation scenario. We further considered an escalated treatment, adding 10 Gy to the photon irradiation with the same fractionation schedule. Generally, increasing dose increases TCP as expected, but it is still less effective than carbon ion treatments (Figure 7 a and b). Gain in TCP is

often insufficient to reach clinically acceptable values. Indeed, considering treatments with TCP ≥ 0.85 as successful, the 10 Gy boost satisfied the condition in 42% of the cases, while the photons reached 30% without the boost (Figure 7c). The increase in TCP is ineffective when met with poor microvascular morphology and, consequently, strong hypoxia (Figure 7d).

The benefit becomes insignificant when the vascular index is 5 or higher. This approach also sheds light on dose-boosting techniques, showing the potential gain with a local dose increase of 10 Gy. On the contrary, carbon ions prove effective in 95% of the cases in our data set, with a tumor control probability (TCP) of 0.85 or higher. The exceptions have a vascular index of 6, representing the least favorable vascular condition in our study.

We note that even if we considered a fractionated scheme, we did not include the effect of radiation damage on vascular damage (e.g., on permeability of the vascular wall and vasodilation). Vascular damage is essential, especially when considering high doses, but we still have limited knowledge of its mechanisms and impact on treatments [42]. We did not consider the reoxygenation effect, namely the possible changes in oxygen consumption during treatment related to cell death. Including this effect and cell proliferation would increase the relevance of this work in the clinic. To this end, a detailed description of the dynamics of cell number due to growth and treatment is required, both through oxygen-mediated mechanisms [34]. The extreme hypoxia scenario can be intensified, leading to a decrease in the flow rate to a non-flow state. To obtain reliable results in this extreme condition, more intricate vascular geometry must be taken into account, as suggested by Schiavo et al. [62].

On the other hand, we consider the average value to be representative of the voxel. Different techniques could be applied and developed to provide a more physics-based extraction of the representative value (e.g., tracer binding kinetics or cellular composition [23]). An example of this application in a different field is the study by Geady et al., in which they evaluated the resolution requirements for radiomic features to be representative of cell biology, considering a physics-based downsampling technique [17]. With a similar approach, we could further evaluate how a specific image (e.g., PET) is representative of the microscopic oxygen distribution.

Summarizing, we discuss how the microvasculature plays a critical role in determining hypoxia at a small scale, analyzing a domain comparable to a single imaging voxel. In fact, variations in vascular density and morphology result in highly heterogeneous oxygenation conditions (Figures 1, 4 and 5). Taking into account the crucial role of oxygen in radiation therapy, vascular networks significantly influence treatment outcomes, measured by tumor control probability (TCP, Figures 6f and 7b). This influence is particularly pronounced for photons and protons, which exhibit similar responses. TCP decreases when unfavorable vascular scenarios are considered. On the contrary, carbon ions demonstrate notably greater efficacy even in such cases. Furthermore, we have observed a strong correlation between TCP and subvoxel hypoxic volume (Figure 6e). However, this correlation relies on sub-voxel data, which are not directly obtainable from images. When restricting our analysis to the average voxel, this correlation dissipates (Figure 6c), highlighting the existence of a resolution gap between imaging capabilities and oxygenation phenomena. The findings suggest that without considering the microscale variability of oxygenation, voxel-based imaging data may lead to underestimating the presence of hypoxic niches that are critical in determining radiation therapy success. This has profound implications for the clinical application of dose painting, necessitating caution in local dose de-escalation strategies.

5 Conclusion

We introduced an advanced computational approach based on multiscale modeling to investigate oxygenation in the tumor microenvironment, accounting for various conditions and vascular properties. Using this model, we can quantitatively assess the influence of several critical factors, including the morphological characteristics of the vascular network. Interestingly, the vascular network significantly affects the efficacy of photon and proton radiotherapy treatment, whereas carbon ion treatment remains effective even with irregular low-density vessel distribution. Proton treatment does not demonstrate a distinct advantage over photon-based radiation therapy in addressing tumor hypoxia.

Our results support the existence of a resolution gap in current clinical imaging [23]. Considering the potential misidentification of hypoxic regions, these findings advise caution when contemplating de-escalation in dose painting.

Furthermore, this computational tool shows promise in evaluating hypothetical scenarios and in vitro models of radiation-induced damage to the microvasculature [25].

Acknowledgments

This work was supported by the AIRC Investigator Grant, no. IG21479 (TZ is the PI of the study). Paolo Zunino acknowledges the support of the grant MUR PRIN 2022 No. 2022WKWZA8 "Immersed methods for multiscale and multiphysics problems (IMMEDIATE)" part of the Next Generation EU program. Piermario Vitullo and Paolo Zunino are members of Gruppo Nazionale per il Calcolo Scientifico (GNCS) of Istituto Nazionale di Alta Matematica (INdAM). The present research is part of the activities of the Dipartimento di Eccellenza 2023-2027, Department of Mathematics, Politecnico di Milano. Sponsors had no role in study design, data collection and analysis, decision to publish or manuscript preparation.

A Parameter estimation for radiobiological models

This supplementary section describes the procedure to fit parameters for the Tinganelli model (TIN) based on data published by Wenzl et al. The TIN model reads as follows:

$$\begin{aligned} OER(0,\ LET) &= \frac{LET^{\gamma} + M\ a}{a + LET^{\gamma}} \\ OER(pO_2,\ LET) &= \frac{b\ OER(0,\ LET) + pO_2}{b + pO_2} \\ D(pO_2,\ LET) &= \frac{D_{ph}}{OER(pO_2,\ LET)} \end{aligned} \tag{14}$$

where M, a, γ, and b are parameters fitted to experimental data.

We first estimate the parameters M, a, and γ by RMSE minimization against the data reported in Figure 1 (solid line) by Wenzl et al. [79] (Figure S10). This data set represents the OER-LET relation under no oxygen conditions ($p_{O_2} = 0.01 mmHg \simeq 0.001\%$). Therefore, we use this data set to estimate $OER(0,\ LET)$. The parameter values are $M = 2.81$, $a = 522.45\ keV/\mu m$, and $\gamma = 1.38$.

As a second step, using the data in Figure 3 of the same work, we estimate the parameter b (Figure S10). We run the RMSE minimization on the data for $LET = 2\ keV/\mu m$. Consequently, the fit is less accurate for $LET = 100\ keV/\mu m$. The resulting value for b is $1.24\ mmHg$.

Finally, we report the OER function considering photon, protons, and carbon, namely $OER_{photons}(pO_2,\ 2\ keV/\mu m)$, $OER_{protons}(pO_2,\ 4\ keV/\mu m)$, and $OER_{carbon}(pO_2,\ 75\ keV/\mu m)$ (Figure S10).

B Numerical discretization and solvers

The discretization of the problem $\mathcal{F} + \mathcal{H} + \mathcal{O}$ is achieved using the finite element method. One of the main advantages of our formulation is that the computational meshes of Ω and Λ are entirely independent. For this reason, we address the two approximations separately.

We denote with $\mathcal{T}_t^h$ an admissible family of partitions of $\bar{\Omega}$ into tetrahedrons K

$$\bar{\Omega} = \bigcup_{K \in \mathcal{T}_t^h} K,$$

that satisfies the usual conditions of a conforming triangulation of Ω. Here, h denotes the characteristic size of the mesh, that is, $h = \max_{K \in \mathcal{T}_t^h} h_K$, where h_K is the diameter of the simplex K. Moreover, we

implicitly assume that Ω is a *polygonal* domain. The solution of $\mathcal{F}$ is approximated using discontinuous piecewise-polynomial finite elements for pressure and $\boldsymbol{H}_{div}$-conforming *Raviart-Thomas* finite elements for velocity, namely

$$Y_k^h := \{v_h \in L^2(\Omega),\ v_h|_K \in P_k(K) \quad \forall K \in \mathcal{T}_t^h\},$$
$$\boldsymbol{RT}_k^h := \{\mathbf{w}_h \in \boldsymbol{H}_{div}(\Omega),\ \mathbf{w}_h|_K \in P_k(K;\mathbb{R}^d) \oplus \mathbf{x}\, P_k(K) \quad \forall K \in \mathcal{T}_t^h\},$$

for every integer $k \geq 0$, where $\mathcal{P}_k$ indicates the standard space of polynomials of degree $\leq k$ in the variables $\mathbf{x} = (x_1, \ldots, x_d)$. The lowest order *Raviart-Thomas* approximation has been adopted, corresponding to $k = 0$ above.

Concerning the capillary network, we adopt the same approach used at the continuous level and split the network branches into separate subdomains. Furthermore, each curved branch Λ_i is approximated by a piecewise linear 1D line, denoted by Λ_i^h. More precisely, the latter is a partition of the i-th branch of the network of a sufficiently large number of segments, named $S \subset \Lambda_i^h$. In this way, we obtain the following discrete domain:

$$\Lambda^h = \bigcup_{i=1}^{N} \Lambda_i^h \,.$$

The solution of $\mathcal{F}$ on a given branch Λ_i^h is approximated using continuous piecewise polynomial finite element spaces for both pressure and velocity. Since we want the vessel velocity to be discontinuous at multiple junctions, we define the finite element space over the whole network as the collection of the local spaces of the single branches. In contrast, pressure has been assumed to be continuous over the network; therefore, its finite element approximation is standard. We will use the following families of finite element spaces for pressure and velocity, respectively:

$$X_{k+1}^h(\Lambda) := \{w_h \in C^0(\bar{\Lambda}),\, w_h|_S \in P_{k+1}(S) \quad \forall S \in \Lambda^h\},$$
$$W_{k+2}^h(\Lambda) := \bigcup_{i=1}^{N} X_{k+2}^h\left(\Lambda_i^h\right),$$

for every integer $k \geq 0$. As a result, we use generalized Taylor-Hood elements on each network branch, satisfying the local stability of the mixed finite element pair for the network in this way. At the same time, we guarantee that the pressure approximation is continuous throughout the network Λ^h. In particular, for the numerical experiments shown later, we have used the lowest order $k = 0$.

For hematocrit, we proceed as we did for the velocity approximation. In particular, we approximate equation $\mathcal{H}$ with the finite element space W_{k+2}^h defined in Λ_i^h. For the sake of generality, let us define the families of discrete subspaces of the functional spaces for $k \geq 0$:

$$\boldsymbol{V}_t^h = \boldsymbol{RT}_k^h(\Omega) \quad \text{and} \quad Q_t^h = Y_k^h(\Omega)\,,$$
$$V_v^h = W_{k+2}^h(\Lambda^h) \quad \text{and} \quad Q_v^h = X_{k+1}^h(\Lambda^h) \quad \text{and} \quad W_v^h = W_{k+2}^h(\Lambda^h)\,.$$

According to work presented in [52, 53], to which we remand for the meaning of all the symbols of the equations that follow, the discrete equations for the microvascular flow and red blood cell transport (the

$\mathcal{F}+\mathcal{H}$ model) are the following: find $\boldsymbol{u}_t^h \in \mathbf{V}_t^h$, $p_t^h \in Q_t^h$, $u_v^h \in V_v^h$, $p_v^h \in Q_v^h$, $H^h \in W_v^h$ such that

$$
\begin{cases}
\left(\nabla\cdot\boldsymbol{u}_t^h\,,\,q_t^h\right)_\Omega - \left(2\pi R f(\overline{p}_t^h,\overline{p}_v^h)\delta_\Lambda\,,\,q_t^h\right)_\Omega = 0 & \forall q_t^h \in Q_t^h,\\[2ex]
\frac{\mu_t}{K}\left(\boldsymbol{u}_t^h\,,\,\boldsymbol{v}_t^h\right)_\Omega - \left(p_t\,,\,\nabla\cdot\boldsymbol{v}_t^h\right)_\Omega = -\left(g_t\,,\,\boldsymbol{v}_t^h\cdot\boldsymbol{n}_t\right)_{\partial\Omega} & \forall \boldsymbol{v}_t^h \in \boldsymbol{V}_t^h,\\[2ex]
\sum_i \left(\partial_s(\pi R_i^2\overline{u}_{v,i}^h\,,\,q_v^h\right)_{\Lambda_i^h}\\
\qquad + \sum_i \left(2\pi R f(\overline{p}_t^h,\overline{p}_v^h)\,,\,q_v^h\right)_{\Lambda_i^h} - \sum_{i\in\mathcal{E}} q_v^h \pi R_i^2 \overline{u}_{v,i}^h|_{\boldsymbol{z}_i}\\
\qquad - \sum_j q_v^h|_{\boldsymbol{y}_j}\left[\sum_{i\in\mathcal{K}_j^+}\pi R_i^2\overline{u}_{v,i}^h|_{\boldsymbol{y}_j} - \sum_{i\in\mathcal{K}_j^-}\pi R_i^2\overline{u}_{v,i}^h|_{\boldsymbol{y}_j}\right] = 0 & \forall q_v^h \in Q_v^h,\\[2ex]
\sum_i\Big(-2\frac{\mu_{v,i}}{R_i^2}\phi'(1)\big(1+\kappa_i^2R_i^2\big)\pi R_i^2\overline{u}_{v,i}^h\,,\,v_{v,i}^h\Big)_{\Lambda_i}\\
\qquad - \sum_i\left(\overline{p}_v^h\,,\,\partial_s(\pi R_i^2 v_{v,i}^h)\right)_{\Lambda_i^h} + \sum_{i\in\mathcal{E}}\overline{p}_v^h\,\pi R_i^2 v_v^h|_{\boldsymbol{z}_i}\\
\qquad + \sum_j \overline{p}_v^h|_{\boldsymbol{y}_j}\left[\sum_{i\in\mathcal{K}_j^+}\pi R_i^2 v_{v,i}^h|_{\boldsymbol{y}_j} - \sum_{i\in\mathcal{K}_j^-}\pi R_i^2 v_{v,i}^h|_{\boldsymbol{y}_j}\right]\\
\qquad = -\sum_{i\in\mathcal{B}}\left[g_v^+\,\pi R_i^2 v_v^h|_{\boldsymbol{x}_i^+} - \,g_v^-\,\pi R_i^2 v_v^h|_{\boldsymbol{x}_i^-}\right] & \forall v_v^h \in V_v^h,\\[2ex]
-\sum_i\left(\pi R_i^2\overline{u}_{v,i}^h H_i^h\,,\,\partial_s w_i^h\right)_{\Lambda_i^h} + \sum_j\sum_{i\in\mathcal{K}^{out}}\pi R_i^2\overline{u}_{v,i}^h H_i^h w_i^h|_{\boldsymbol{y}_j}\\
\qquad + \sum_{i\in\mathcal{B}}\pi R_i^2\overline{u}_{v,i}^h H_i^h w_i^h|_{\boldsymbol{x}_i^{out}} + \sum_{i\in\mathcal{E}}\pi R_i^2\overline{u}_{v,i}^h H_i^h w_i^h|_{\boldsymbol{z}_i}\\
\qquad - \sum_j\sum_{i\in\mathcal{K}_j^{in}} F_{QE,j,i} w_i^h|_{\boldsymbol{y}_j}\left(\sum_{i\in\mathcal{K}_j^{out}}\pi R_i^2\overline{u}_{v,i}^h H_i^h|_{\boldsymbol{y}_j}\right)\\
\qquad = \sum_j\sum_{i\in\mathcal{B}}\pi R_i^2\overline{u}_{v,i}^h H_0 w_i^h|_{\boldsymbol{x}_i^{in}} & \forall w_i^h \in W_v^h\,.
\end{cases}
$$

Similarly, the discrete formulation of the oxygen transport problem, namely the problem $\mathcal{O}$, is obtained by projecting the weak formulation of the equations in suitable discrete finite element spaces.

Let us define $Q_t^h = Y_k^h(\Omega)$ and $Q_v^h = X_k^h(\Lambda)$ for k ≥ 0 where $Y_k^h := \{f_h \in C^0(\Omega),\ f_h|_K \in P_k(K) \quad \forall K \in \mathcal{T}_t^h\}$, for every integer $k \geq 0$, where P_k indicates the standard space of polynomials of degree $\leq k$ in variables $\mathbf{x} = (x_1, \ldots, x_d)$ and $X_k^h(\Lambda) := \{g_h \in C^0(\Lambda),\ g_h|_S \in P_k(S) \quad \forall S \in \Lambda^h\}$, for every integer $k \geq 0$.

We also apply a fixed-point method to linearize the system of equations by evaluating the reaction term in the tissue and the oxyhemoglobin concentration in the microvessels at the previous iteration. More precisely, we define the new coefficient, $\Psi^{(k-1)}$ as the oxyhemoglobin concentration at the previous iteration:

$$\Psi^{(k-1)} = k_1\ H\ \frac{\left(C_v^{(k-1)}\right)^{\gamma-1}}{\left(C_v^{(k-1)}\right)^{\gamma} + k_2}$$

Such formulation of the oxyhemoglobin term highlights the effect of free oxygen transport with respect to hemoglobin-bound oxygen. Then, the blood velocity can be re-written as follows:

$$u_v^{h,(k-1)} = u_v^h\ (1 + \Psi^{(k-1)});$$

Then, the discrete equations for the oxygen transport model become: find $C_t^{h,(k)} \in Q_t^h$ and $C_v^{h,(k)} \in Q_v^h$

such that,

$$\begin{cases} (D_t \nabla C_t^{h,(k)},\ \nabla q_t^h)_\Omega + (\nabla \cdot (\mathbf{u}_t C_t^{h,(k)}),\ q_t^h)_\Omega + (\beta_{O_2} C_t^{h,(k)}, q_t^h)_{\partial\Omega} \\ \quad - \left(\left[2\pi R\ P_{O_2}(C_v^{h,(k)} - \boldsymbol{ct}) + \frac{\phi_v}{2}\ \left(C_v^{h,(k)} + \boldsymbol{ct} \right) \right], \overline{q}_t \right)_\Lambda \\ \quad + \left(\frac{V_{max}}{C_t^{h,(k-1)} + \alpha_t p^{m_5 0}}\ C_t^{h,(k)},\ q_t^h \right)_\Omega = (\beta_{O_2} c_{0,t}, q_t^h)_{\partial\Omega}\,, \quad \forall q_t^h \in Q_t^h \\ \\ \left(\pi R^2 D_v\ \frac{\partial C_v^{h,(k)}}{\partial s}, \frac{\partial q_v^h}{\partial s} \right)_\Lambda + \left(\pi R^2 u_v^{h,(k-1)}\ C_v^{h,(k)}, q_v^h \right)_\Lambda \\ \quad + \left(\left[2\pi R\ P_{O_2}(C_v^{h,(k)} - \boldsymbol{ct}) + \frac{\phi_v}{2} \left(C_v^{h,(k)} + \boldsymbol{ct} \right) \right], q_v^h \right)_\Lambda = 0 \quad \forall q_v^h \in Q_v^h. \end{cases}$$

As mentioned above, the meaning of all variables and symbols of these equations is described in [51].

To calculate the numerical solution of the problem, let us introduce the algebraic formulation of the complete problem. Linearization of the problem is beneficial. At each stage of the fix-point technique, a linear system is generated and must be solved. To be more concise, we report the complete formulation of the discrete system only for the oxygen transport problem $\mathcal{O}$, remanding to the interested reader the discrete version of $\mathcal{F} + \mathcal{H}$ to [52].

For problem $\mathcal{O}$, the number of degrees of freedom (DOF) of the discrete spaces Q_t^h and Q_v^h is $N_t^h = dim(Q_t^h)$ and $N_v^h = dim(Q_v^h)$ and the finite element basis functions are $\{\varphi_t^i\}_{i=1}^{N_t^h}$ for Q_t^h and $\{\varphi_v^j\}_{j=1}^{N_v^h}$ for Q_v^h. Then the numerical solution for the oxygen concentration can be written as a linear combination of these base functions $C_t^h(\mathbf{x}) = \sum_{i=1}^{N_t^h} {c_t}^{h,i(k)}\ \varphi_t^i(\mathbf{x}), \quad \forall \mathbf{x} \in Q_t^h\ C_v^h(s) = \sum_{j=1}^{N_v^h} {c_v}^{h,j(k)}\ \varphi_v^j(s)$. Substituting these expressions in the weak discrete problem and exploiting the linearity of the inner product, we obtain the following linear system for each iterative step:

$$\begin{bmatrix} \mathbb{D}_t + \mathbb{A}_t + \mathbb{R}_t + \mathbb{B}_{tt} & \mathbb{B}_{tv} \\ \mathbb{B}_{vt} & \mathbb{D}_v + \mathbb{A}_v + \mathbb{B}_{vv} \end{bmatrix} \begin{bmatrix} \mathbf{C}_t^{h(k)} \\ \mathbf{C}_v^{h(k)} \end{bmatrix} = \begin{bmatrix} \mathbb{F}_t \\ \mathbb{F}_v \end{bmatrix}. \tag{15}$$

The submatrices and subvectors in (15) are defined as follows:

$$[\mathbb{D}_t]_{ij} := (D_t^*\ \boldsymbol{\varphi}_t^j, \boldsymbol{\varphi}_t^i)_\Omega + (\beta_t \boldsymbol{\varphi}_t^j, \boldsymbol{\varphi}_t^i)_{\partial\Omega_{MIX}}, \qquad \mathbb{D}_t \in \mathbb{R}^{N_t^h \times N_t^h},$$

$$[\mathbb{A}_t]_{ij} := (\boldsymbol{u_t^h} \cdot \nabla \boldsymbol{\varphi}_t^j, \boldsymbol{\varphi}_t^i)_\Omega + (\nabla \cdot \boldsymbol{u_t^h}\ \boldsymbol{\varphi}_t^j, \boldsymbol{\varphi}_t^i)_\Omega, \qquad \mathbb{A}_t \in \mathbb{R}^{N_t^h \times N_t^h},$$

$$[\mathbb{R}_t]_{ij} := (\frac{M_0}{C_t^{h,(k-1)} + K_M}\ \boldsymbol{\varphi}_t^j, \boldsymbol{\varphi}_t^i)_\Omega, \qquad \mathbb{R}_t \in \mathbb{R}^{N_t^h \times N_t^h},$$

$$[\mathbb{D}_v]_{ij} := (\pi R^{*2} D_v^*\ \frac{\partial \boldsymbol{\varphi}_v^j}{\partial s}, \frac{\partial \boldsymbol{\varphi}_v^i}{\partial s})_\Omega, \qquad \mathbb{D}_v \in \mathbb{R}^{N_v^h \times N_v^h},$$

$$[\mathbb{A}_v]_{ij} := (\pi R^{*2}\ u_v^{*h,(k-1)} \frac{\partial \boldsymbol{\varphi}_v^j}{\partial s}, \boldsymbol{\varphi}_v^i)_\Omega + (\pi R^{*2}\ \frac{\partial u_v^{*h,(k-1)}}{\partial s} \boldsymbol{\varphi}_v^j, \boldsymbol{\varphi}_v^i)_\Omega + \qquad \mathbb{A}_v \in \mathbb{R}^{N_v^h \times N_v^h},$$

$$+ (\pi R^{*2}\ \beta_v \boldsymbol{\varphi}_v^j, \boldsymbol{\varphi}_v^i)_{\partial\Lambda_{OUT}},$$

$$[\mathbb{B}_{tt}]_{ij} := -(2\pi R^*[P_l^* + \frac{L_p^*}{2}\ P\ (P_v - P_t - \sigma\Delta\pi)]\boldsymbol{\varphi}_t^j, \boldsymbol{\varphi}_t^i)_\Omega, \qquad \mathbb{B}_{tt} \in \mathbb{R}^{N_t^h \times N_t^h},$$

$$[\mathbb{B}_{tv}]_{ij} := +(2\pi R^*[P_l^* + \frac{L_p^*}{2}\ P\ (P_v - P_t - \sigma\Delta\pi)]\boldsymbol{\varphi}_t^j, \boldsymbol{\varphi}_v^i)_\Omega, \qquad \mathbb{B}_{tv} \in \mathbb{R}^{N_t^h \times N_v^h},$$

$$[\mathbb{B}_{vv}]_{ij} := -(2\pi R^*[P_l^* + \frac{L_p^*}{2}\ P\ (P_v - P_t - \sigma\Delta\pi)]\boldsymbol{\varphi}_v^j, \boldsymbol{\varphi}_v^i)_\Omega, \qquad \mathbb{B}_{vv} \in \mathbb{R}^{N_v^h \times N_v^h},$$

$$[\mathbb{B}_{vt}]_{ij} := +(2\pi R^*[P_l^* + \frac{L_p^*}{2}\ P\ (P_v - P_t - \sigma\Delta\pi)]\boldsymbol{\varphi}_v^j, \boldsymbol{\varphi}_t^i)_\Omega, \qquad \mathbb{B}_{vt} \in \mathbb{R}^{N_v^h \times N_t^h},$$

$$[\mathbb{F}_t]_i := -(\beta_t\ c_{0,t}\ \boldsymbol{\varphi}_t^i)_{\partial\Omega_{MIX}}, \qquad \mathbb{F}_t \in \mathbb{R}^{N_t^h},$$

$$[\mathbb{F}_v]_i := -(\pi R^{*2}\ \beta_v\ c_{0,v}\ \boldsymbol{\varphi}_v^i)_{\partial\Lambda_{OUT}}, \qquad \mathbb{F}_v \in \mathbb{R}^{N_v^h}.$$

Where u_v^* is:

$$u_v^{*(k-1)} = u_v\ (1 + k_1\ H\ \frac{C_v^{(k-1)^{\gamma-1}}}{C_v^{(k-1)^\gamma} + k_2})$$

Table 1: **Values for the parameters of the model.** The values of the parameters are reported along with their units and references. Parameters specified for the oxygen scenarios are changed, while the others remain constant.

Network morphology			
Symbol	**Parameter**	**Value**	**Ref.**
S/V	Vascular area over tissue volume	$3500 - 7000 - 14000\ m^{-1}$	[3]
d_{max}	Maximum distance from the network	$120 - 160 - 240\ \mu m$	-
Fluid problem $\mathcal{F}$			
K	Tissue permeability	$3.6 \times 10^{-17}\ m^2$	[69]
μ_t	Interstitial fluid viscosity	$1.2 \times 10^{-3}\ Pa\,s$	[72]
μ_v	Blood viscosity	computed	[55]
R	Vascular radius	variable	[77]
Lp	Vascular wall hydraulic conductivity	$1.4 \times 10^{-10}\ m^2 s/kg$	[59]
$\pi_v - \pi_t$	Transmural osmotic difference	$640\ Pa$	[73, 32]
σ	Reflection coefficient for proteins	0.82	[69]
Oxygen problem $\mathcal{O}$			
HF	Hüfner factor	$1.36\ ml_{O_2}/g_{Hb}$	[78]
$MCHC$	Mean Corpuscular Hematocrit Concentration	$0.34\ g_{Hb}/ml_{RBC}$	[78]
η_{pl}	Oxygen solubility in plasma	$2.82 \times 10^{-5}\ (ml_{O_2}/ml)/mmHg$	[43]
$p_{s_{50}}$	pO_2 at hemoglobin half-saturation	$27\ mmHg$	[78]
γ_{Hb}	Hill exponent	2.64	[78]
V_{max}	Maximum oxygen consumption rate	$2.47 \times 10^{-4}\ (ml_{O_2}/s)/cm^3$	[78]
η_t	Oxygen solubility in tissue	$3.89 \times 10^{-5}\ (ml_{O_2}/cm^3)/mmHg$	[43]
$p_{m_{50}}$	pO_2 at half consumption rate	$0.5\ mmHg$	[78, 43]
P_{O_2}	Microvascular wall permeability	$3.5 \times 10^{-5}\ m/s$	[6]
ε_t	Oxygen diffusion coefficient in tissue	$2.41 \times 10^{-9}\ m^2/s$	[43]
ε_v	Oxygen diffusion coefficient in vasculature	$2.18 \times 10^{-9}\ m^2/s$	[43]
Boundary conditions			
$p_v\|_{in}$	Pressure at vascular inlets	$40\ mmHg$	[41]
$p_v\|_{out}$	Pressure at vascular outlets	$15\ mmHg$	[41]
H_{in}	Discharge hematocrit at vascular inlets	0.45	[78]
$pO_2\|_{in}$	pO_2 at vascular inlets	$90\ mmHg$	[60, 44, 47]
Radiotherapy			
N	Tumor cells in reference volume	$15k$	[48]
a_1	WEN parameter	$0.22\ Gy^{-1}$	[79]
a_2	WEN parameter	$0.0024\ Gy^{-1}(keV/\mu m)^{-1}$	[79]
a_3	WEN parameter	$0.05\ Gy^{-1}$	[79]
a_4	WEN parameter	$0.0031\ Gy^{-1}(keV/\mu m)^{-1}$	[79]
b_1	WEN parameter	$0.4\ Gy^{-1}$	[79]
b_2	WEN parameter	$0.015\ Gy^{-1}$	[79]
k_{RT}	pO_2 for half radiosensitivity (WEN)	$3\ mmHg$	[79]
γ	TIN parameter	1.38	see Appendix
M	TIN parameter	2.81	see Appendix
a	TIN parameter	$522.45\ keV/\mu m$	see Appendix
b	TIN parameter	$1.24\ mmHg$	see Appendix
Oxygen scenarios			
Symbol	**Parameter**	**Value**	**Scenario**
$p_v\|_{in}$	Pressure at vascular inlets	$30\ mmHg$	Acute hypoxia
$p_v\|_{out}$	Pressure at vascular outlets	$25\ mmHg$	Acute hypoxia
V_{max}	Maximum oxygen consumption rate	$4.94 \times 10^{-4}\ (ml_{O_2}/s)/cm^3$	High consumption

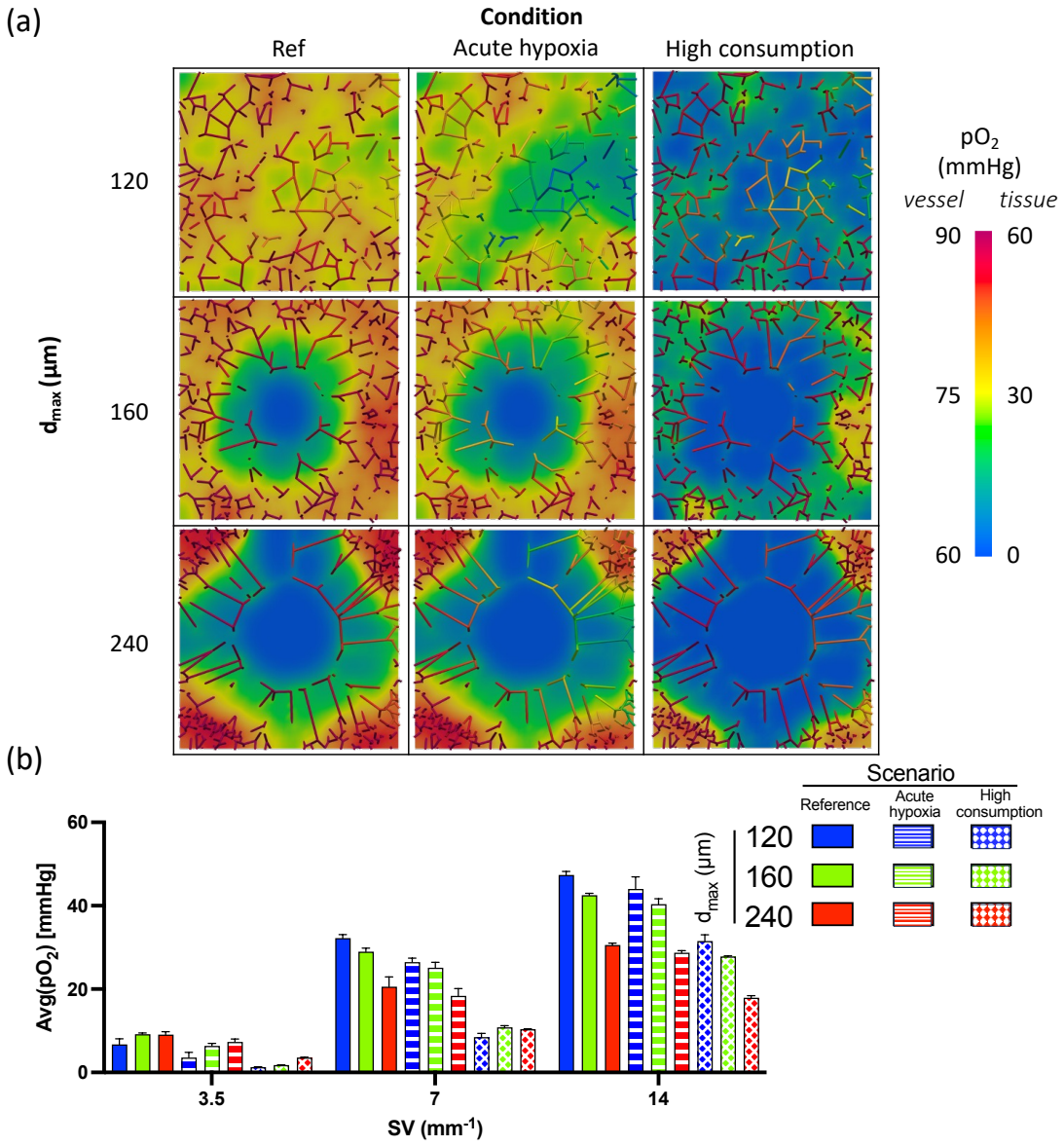

Figure 4: **Oxygen distribution for the different oxygen scenarios** (a) Oxygen maps referring to networks with $S/V = 7\ mm^{-1}$, varying d_{max} in the vertical direction, and oxygen scenarios in the horizontal one. (b) Average oxygen partial pressure in all the 27 cases considered ($3\ S/V \times 3\ d_{max} \times 3\ oxygen\ scenarios$).

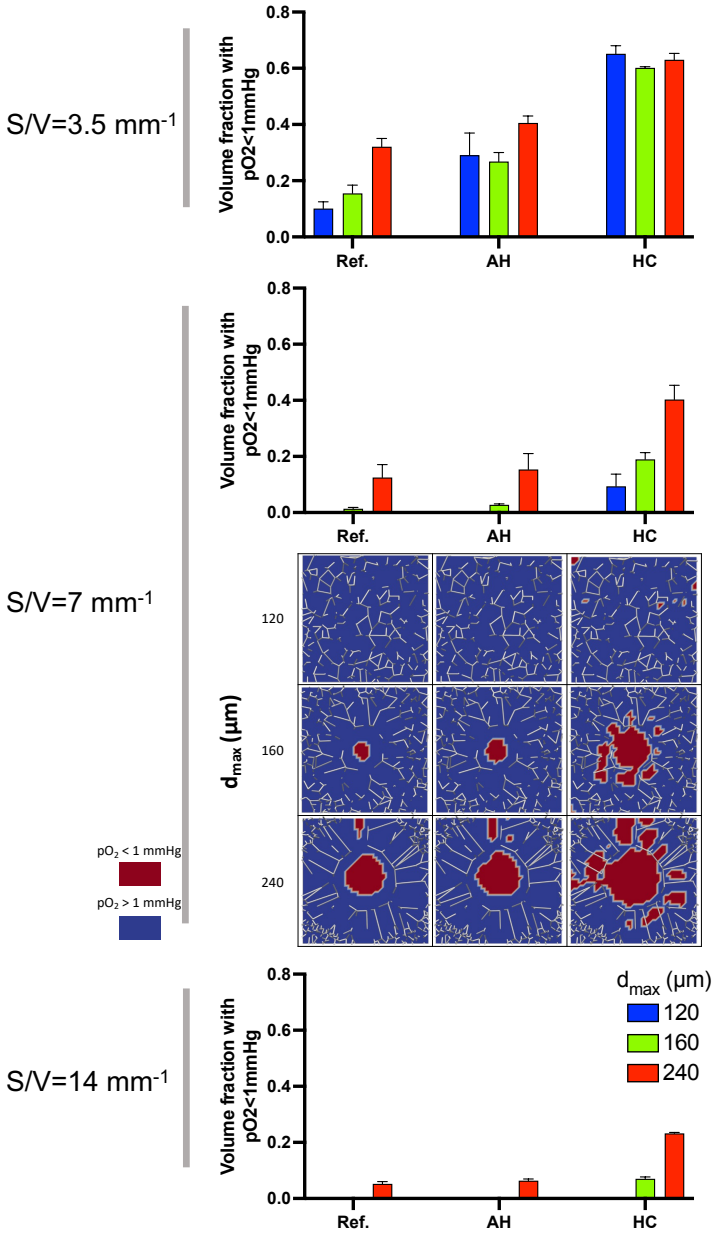

Figure 5: **Hypoxic areas for the different oxygen scenarios** Volume fractions with $pO_2 \leq 1\ mmHg$ in all the 27 cases considered ($3\ S/V \times 3\ d_{max} \times 3\ oxygen\ scenarios$). Plots are complemented by hypoxia maps referring to networks with $S/V = 7\ mm^{-1}$, varying d_{max} in the vertical direction, and oxygen scenarios in the horizontal one.

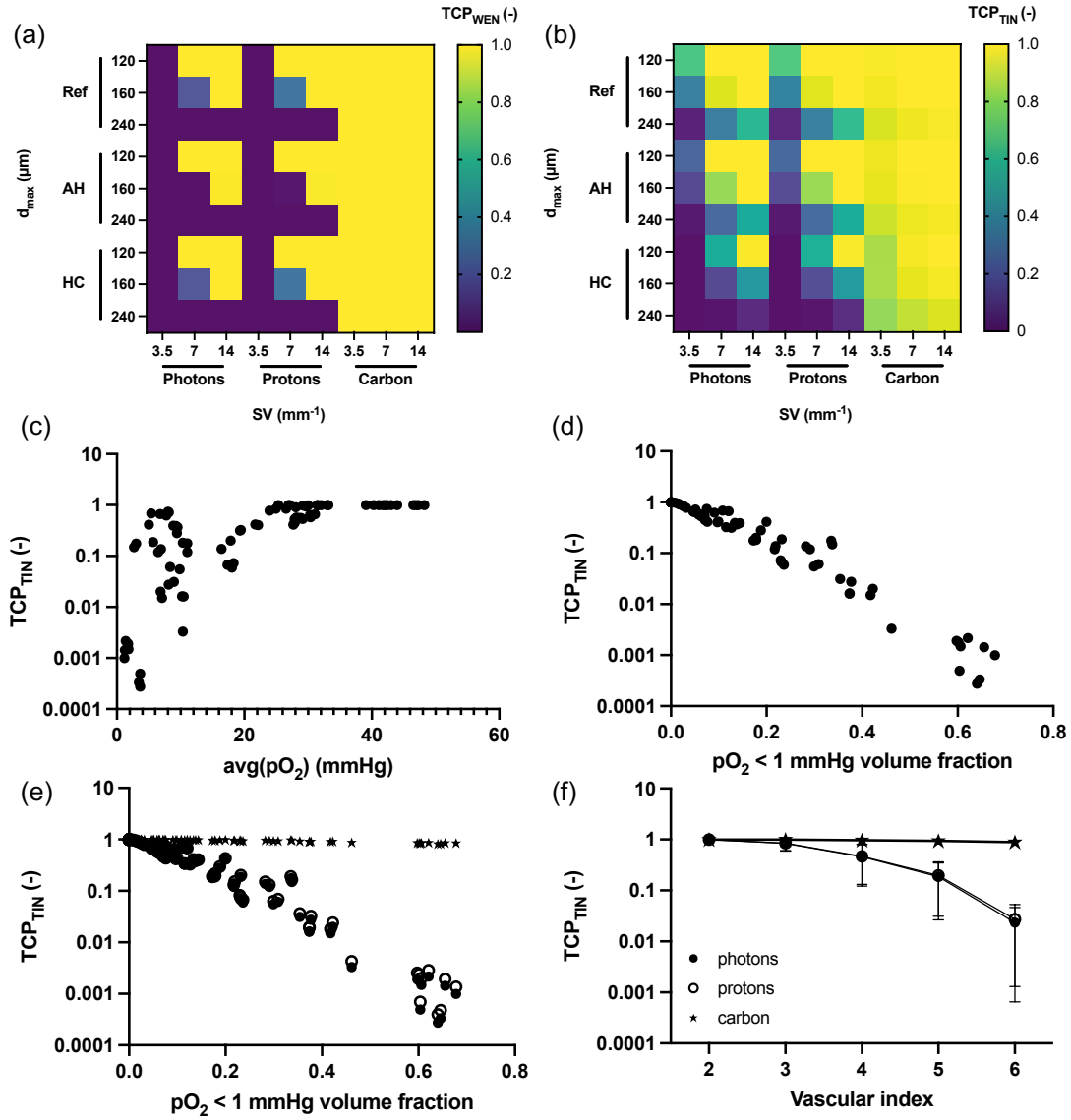

Figure 6: **Irradiation results in all the cases analyzed.** Heat maps with the TCPs for all the cases analyzed with the WEN (a) and the TIN model (b). Ref = Reference cases. AH = Acute Hypoxia cases. HC = High consumption cases. Scatterplot showing the correlation between TCP (computed with the TIN model) with average oxygen partial pressure (c) and hypoxic volume fraction $pO_2 \leq 1\ mmHg$ (d). (e) Scatterplot for TCP and hypoxic volume fraction considering different treatments. (f) Effect of the *vascular index* on the TCP with different treatments.

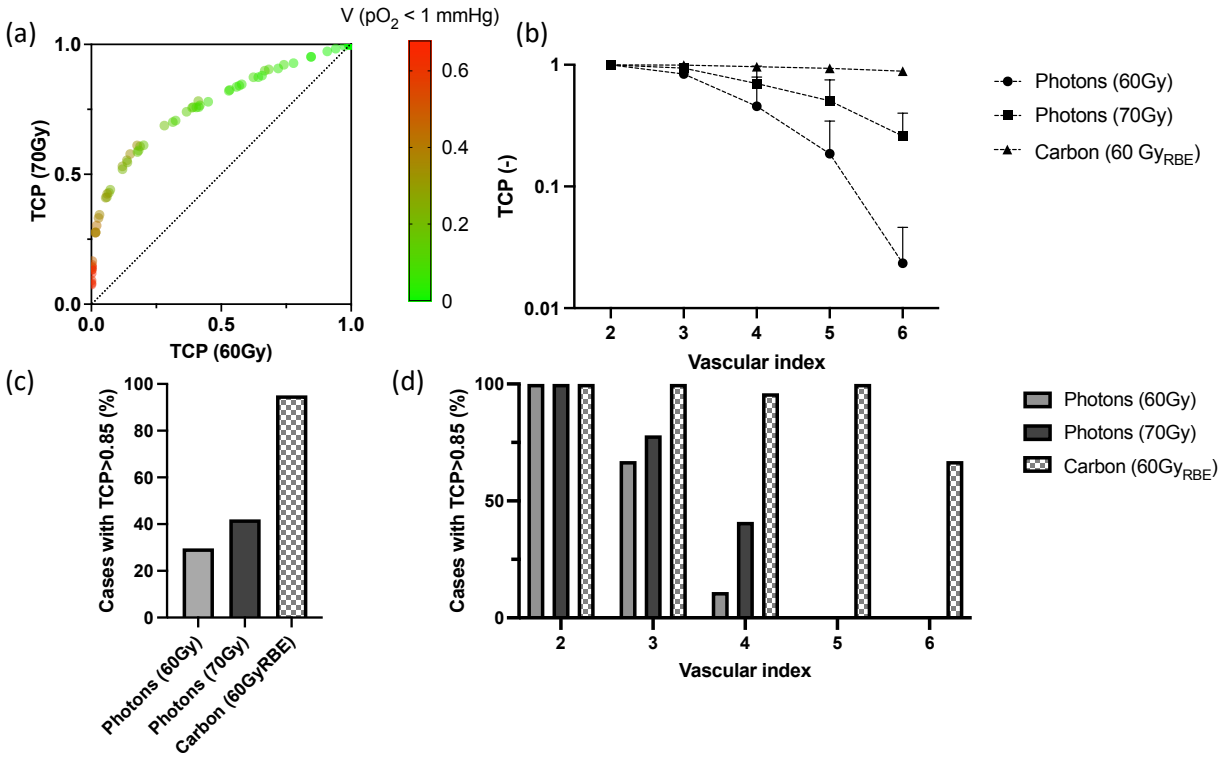

Figure 7: **Effect of 10 Gy boost with photons.** Effect of boosting with 10 Gy photons compared to 60 Gy_{RBE} treatments with photons and carbon ions. (a) Change in TCP with additional boost, colored by the hypoxic volume fraction ($pO_2 \leq 1mmHg$). Each dot represents one of the cases previously described treated with 60 Gy or 70 Gy. (b) TCP variations with vascular index comparing photons, boost with photons, and carbon ions. (c) Percentage of the cases with TCP ≥ 0.85 considering the three treatments applied to the entire dataset and divided by vascular index (d).

C Supplementary figures

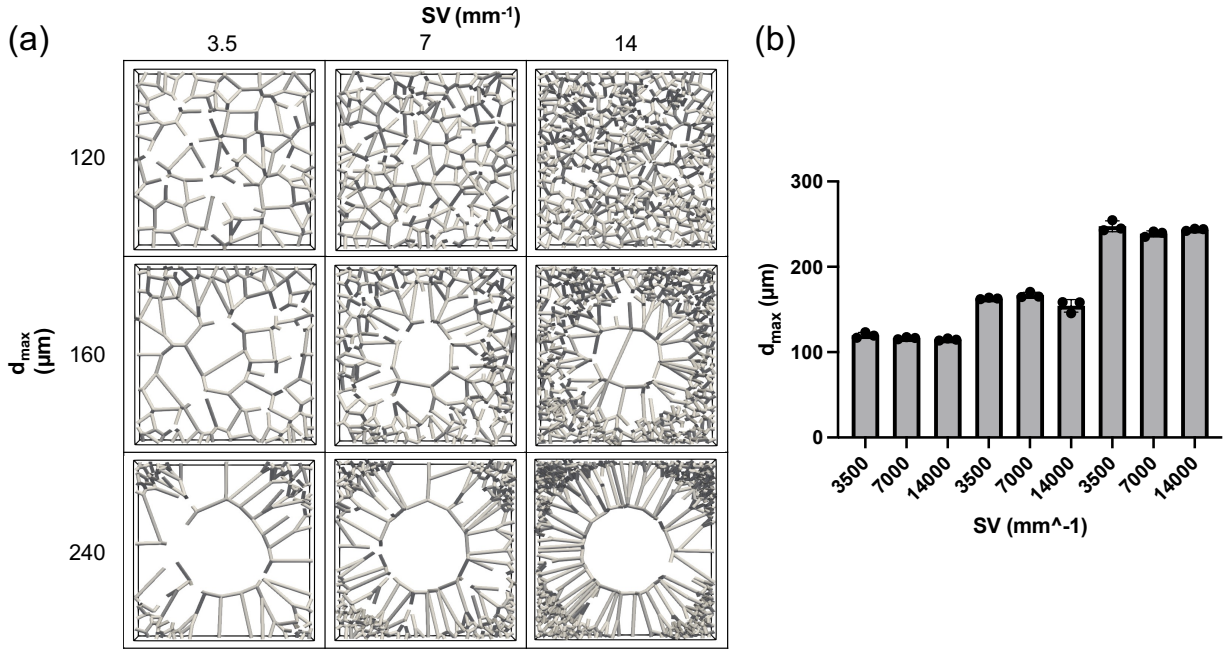

Figure 8: **Set of networks with data.** Representative images of the networks generated in the tissue slab. (a) One replicate per condition illustrating the effect of the two metrics, S/V and d_{max}. (b) Evaluation of S/V and d_{max} for the networks. Columns represent the averages of three samples, each indicated by a single dot.

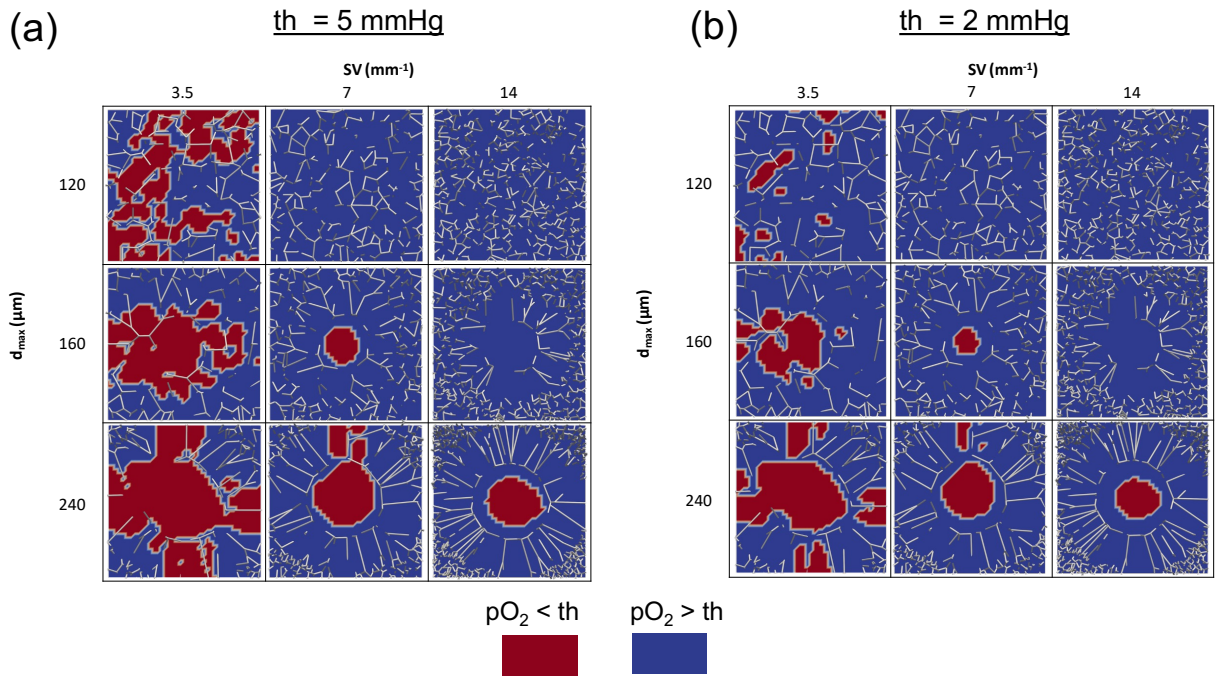

Figure 9: **Spatial distribution of low oxygen areas in the reference scenario.** Low oxygen areas in the nine cases with (a) $th = \ 5mmHg$ and (b) $th = \ 2mmHg$.

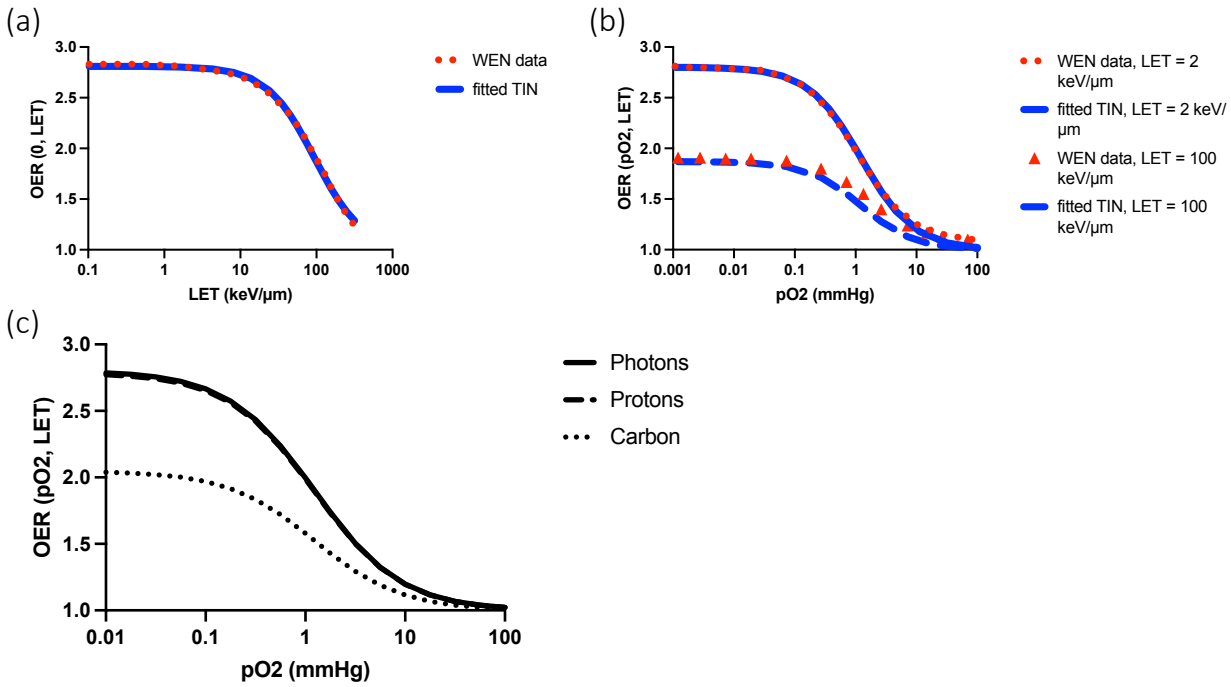

Figure 10: **TIN model fitting against WEN data.** TIN model fitting against WEN data. (a) Fitting for the $OER(0,\ LET)$ function. (b) Fitting for the $OER(pO_2,\ LET)$ relation with $LET = 2\ keV/\mu m$ and $LET = 100\ keV/\mu m$. (c) The resulting OER model for photons, protons, and carbon ions.

References

[1] T. Alper and P. Howard-Flanders. Role of oxygen in modifying the radiosensitivity of e. coli b. *Nature*, 178(4540):978–979, 1956.

[2] L. Antonovic, E. Lindblom, A. Dasu, N. Bassler, Y. Furusawa, and I. Toma-Dasu. Clinical oxygen enhancement ratio of tumors in carbon ion radiotherapy: the influence of local oxygenation changes. *Journal of Radiation Research*, 55:902–911, 9 2014.

[3] Laurence T. Baxter and Rakesh K. Jain. Transport of fluid and macromolecules in tumors. ii. role of heterogeneous perfusion and lymphatics. *Microvascular Research*, 40:246–263, 9 1990.

[4] Kamilla JA. Bigos, Conrado G. Quiles, Sapna Lunj, Danielle J. Smith, Mechthild Krause, Esther GC. Troost, Catharine M. West, Peter Hoskin, and Ananya Choudhury. Tumour response to hypoxia: understanding the hypoxic tumour microenvironment to improve treatment outcome in solid tumours. *Frontiers in Oncology*, 14, 1 2024.

[5] A. Carreau, B.E. Hafny-Rahbi, A. Matejuk, C. Grillon, and C. Kieda. Why is the partial oxygen pressure of human tissues a crucial parameter? small molecules and hypoxia. *Journal of Cellular and Molecular Medicine*, 15(6):1239–1253, 2011.

[6] L. Cattaneo and P. Zunino. A computational model of drug delivery through microcirculation to compare different tumor treatments. *International Journal for Numerical Methods in Biomedical Engineering*, 30(11):1347–1371, 2014.

[7] L. Cattaneo and P. Zunino. Computational models for fluid exchange between microcirculation and tissue interstitium. *Networks and Heterogeneous Media*, 9(1):135–159, 2014.

[8] D. Chapelle, J.-F. Gerbeau, J. Sainte-Marie, and I.E. Vignon-Clementel. A poroelastic model valid in large strains with applications to perfusion in cardiac modeling. *Computational Mechanics*, 46(1):91 – 101, 2010.

[9] Srinivas Chiguru, Rashmi Reddy, Rami Hallac, Joshua Gunpat, Heling Zhou, Saleh Ramezani, Nikolai Slavine, Padmakar Kulkarni, Matthew Lewis, and Ralph Mason. Examining tumor hypoxia using mri (bold/told) in correlation with [18f]fmiso pet. *Journal of Nuclear Medicine*, 54(supplement 2):1138–1138, 2013.

[10] D. De Ruysscher, G. Niedermann, N.G. Burnet, S. Siva, A.W.M. Lee, and F. Hegi-Johnson. Radiotherapy toxicity. *Nature Reviews Disease Primers*, 5(1), 2019.

[11] Simone Di Gregorio, Marco Fedele, Gianluca Pontone, Antonio F. Corno, Paolo Zunino, Christian Vergara, and Alfio Quarteroni. A computational model applied to myocardial perfusion in the human heart: From large coronaries to microvasculature. *Journal of Computational Physics*, 424, 2021.

[12] Marco Durante, Jürgen Debus, and Jay S. Loeffler. Physics and biomedical challenges of cancer therapy with accelerated heavy ions. *Nature Reviews Physics*, 3:777–790, 12 2021.

[13] Ignacio Espinoza, Peter Peschke, and Christian P. Karger. A model to simulate the oxygen distribution in hypoxic tumors for different vascular architectures. *Medical Physics*, 40:081703, 7 2013.

[14] Louis Gagnon, Amy F. Smith, David A. Boas, Anna Devor, Timothy W. Secomb, and Sava Sakadžić. Modeling of cerebral oxygen transport based on in vivo microscopic imaging of microvascular network structure, blood flow, and oxygenation. *Frontiers in Computational Neuroscience*, 10, 2016.

[15] Roberto García-Figueiras, Sandra Baleato-González, Antonio Luna, Anwar R. Padhani, Joan C. Vilanova, Ana M. Carballo-Castro, Laura Oleaga-Zufiria, Juan Antonio Vallejo-Casas, Ana Marhuenda, and Antonio Gómez-Caamaño. How imaging advances are defining the future of precision radiation therapy. *RadioGraphics*, 44(2):e230152, 2024. PMID: 38206833.

[16] Guillermo Garrido-Hernandez, Helge Henjum, Marte Kåstad Høiskar, Tordis Johnsen Dahle, Kathrine Røe Redalen, and Kristian Smeland Ytre-Hauge. Hypoxia adapted relative biological effectiveness models for proton therapy: a simulation study. *Biomedical Physics & Engineering Express*, 8:065026, 11 2022.

[17] C. Geady, H. Keller, I. Siddiqui, J. Bilkey, N.C. Dhani, and D.A. Jaffray. Bridging the gap between micro- and macro-scales in medical imaging with textural analysis – a biological basis for ct radiomics classifiers? *Physica Medica*, 72:142–151, 4 2020.

[18] Inês Godet, Steven Doctorman, Fan Wu, and Daniele M. Gilkes. Detection of hypoxia in cancer models: Significance, challenges, and advances. *Cells*, 11:686, 2 2022.

[19] Florian Goirand, Tanguy Le Borgne, and Sylvie Lorthois. Network-driven anomalous transport is a fundamental component of brain microvascular dysfunction. *Nature Communications*, 12:7295, 12 2021.

[20] Ian G. Gould and Andreas A. Linninger. Hematocrit distribution and tissue oxygenation in large microcirculatory networks. *Microcirculation*, 22(1):1–18, 2015.

[21] GraphPad. Prism, 2024.

[22] David Robert Grimes, Pavitra Kannan, Daniel R. Warren, Bostjan Markelc, Russell Bates, Ruth Muschel, and Mike Partridge. Estimating oxygen distribution from vasculature in three-dimensional tumour tissue. *Journal of The Royal Society Interface*, 13(116):20160070, 2016.

[23] David Robert Grimes, Daniel R Warren, and Samantha Warren. Hypoxia imaging and radiotherapy: bridging the resolution gap. *The British Journal of Radiology*, 90:20160939, 8 2017.

[24] James A. Grogan, Bostjan Markelc, Anthony J. Connor, Ruth J. Muschel, Joe M. Pitt-Francis, Philip K. Maini, and Helen M. Byrne. Predicting the influence of microvascular structure on tumor response to radiotherapy. *IEEE Transactions on Biomedical Engineering*, 64:504–511, 2017.

[25] Zhaobin Guo, Chih Tsung Yang, Michelle F. Maritz, Huanjin Wu, Puthenparampil Wilson, Majid Ebrahimi Warkiani, Chia Chi Chien, Ivan Kempson, Amir R. Aref, and Benjamin Thierry. Validation of a vasculogenesis microfluidic model for radiobiological studies of the human microvasculature. *Advanced Materials Technologies*, 4:1–12, 2019.

[26] Oliver J. Gurney-Champion, Faisal Mahmood, Marcel van Schie, Robert Julian, Ben George, Marielle E.P. Philippens, Uulke A. van der Heide, Daniela Thorwarth, and Kathrine R. Redalen. Quantitative imaging for radiotherapy purposes. *Radiotherapy and Oncology*, 146:66–75, 5 2020.

[27] Grant Hartung, Shoale Badr, Mohammad Moeini, Frédéric Lesage, David Kleinfeld, Ali Alaraj, and Andreas Linninger. Voxelized simulation of cerebral oxygen perfusion elucidates hypoxia in aged mouse cortex. *PLOS Computational Biology*, 17:e1008584, 1 2021.

[28] Tord Hompland, Knut Håkon Hole, Harald Bull Ragnum, Eva-Katrine Aarnes, Ljiljana Vlatkovic, A. Kathrine Lie, Sebastian Patzke, Bjørn Brennhovd, Therese Seierstad, and Heidi Lyng. Combined mr imaging of oxygen consumption and supply reveals tumor hypoxia and aggressiveness in prostate cancer patients. *Cancer Research*, 78:4774–4785, 8 2018.

[29] Michael R. Horsman, Lise Saksø Mortensen, Jørgen B. Petersen, Morten Busk, and Jens Overgaard. Imaging hypoxia to improve radiotherapy outcome. *Nature Reviews Clinical Oncology*, 9:674–687, 12 2012.

[30] Ken ichiro Matsumoto, James B. Mitchell, and Murali C. Krishna. Multimodal functional imaging for cancer/tumor microenvironments based on mri, epri, and pet. *Molecules*, 26:1614, 3 2021.

[31] David A. Jaffray, Felicia Knaul, Michael Baumann, and Mary Gospodarowicz. Harnessing progress in radiotherapy for global cancer control. *Nature Cancer*, 4(9):1228–1238, 2023.

[32] Rakesh K. Jain, Ricky T. Tong, and Lance L. Munn. Effect of vascular normalization by antiangiogenic therapy on interstitial hypertension, peritumor edema, and lymphatic metastasis: Insights from a mathematical model. *Cancer Research*, 67(6):2729–2735, 2007.

[33] M. Jarzyńska. The application of practical kedem-katchalsky equations in membrane transport. *Central European Journal of Physics*, 4(4):429–438, 2006.

[34] J Jeong, K I Shoghi, and J O Deasy. Modelling the interplay between hypoxia and proliferation in radiotherapy tumour response. *Physics in Medicine and Biology*, 58:4897–4919, 7 2013.

[35] Christian P Karger and Peter Peschke. Rbe and related modeling in carbon-ion therapy. *Physics in Medicine & Biology*, 63:01TR02, 12 2017.

[36] Kitware. Paraview, 2024.

[37] Tobias Köppl, Ettore Vidotto, and Barbara Wohlmuth. A 3d-1d coupled blood flow and oxygen transport model to generate microvascular networks. *International Journal for Numerical Methods in Biomedical Engineering*, 36, 10 2020.

[38] F. Laurino and P. Zunino. Derivation and analysis of coupled pdes on manifolds with high dimensionality gap arising from topological model reduction. *ESAIM: Mathematical Modelling and Numerical Analysis*, 53(6):2047–2080, 2019.

[39] Marta Lazzeroni, Ana Ureba, Nicole Wiedenmann, Nils H. Nicolay, Michael Mix, Benedikt Thomann, Dimos Baltas, Iuliana Toma-Dasu, and Anca L. Grosu. Evolution of the hypoxic compartment on sequential oxygen partial pressure maps during radiochemotherapy in advanced head and neck cancer. *Physics and Imaging in Radiation Oncology*, 17:100–105, 1 2021.

[40] J. J. Lee, E. Piersanti, K.-A. Mardal, and M. E. Rognes. A mixed finite element method for nearly incompressible multiple-network poroelasticity. *SIAM Journal on Scientific Computing*, 41(2):A722–A747, 2019.

[41] J. Rodney Levick and C. Charles Michel. Microvascular fluid exchange and the revised starling principle. *Cardiovascular Research*, 87:198–210, 2010.

[42] EMELY KJELLSSON LINDBLOM, SUSANTA HUI, JAMISON BROOKS, ALEXANDRU DASU, MACIEJ KUJAWSKI, and IULIANA TOMA-DASU. Radiation-induced vascular damage and the impact on the treatment outcome of stereotactic body radiotherapy. *Anticancer Research*, 39:2721–2727, 6 2019.

[43] A. Lücker, B. Weber, and P. Jenny. A dynamic model of oxygen transport from capillaries to tissue with moving red blood cells. *American Journal of Physiology - Heart and Circulatory Physiology*, 308(3):H206–H216, 2015.

[44] Adrien Lücker, Timothy W. Secomb, Bruno Weber, and Patrick Jenny. The relative influence of hematocrit and red blood cell velocity on oxygen transport from capillaries to tissue. *Microcirculation*, 24:e12337, 4 2017.

[45] S.J. McMahon. The linear quadratic model: Usage, interpretation and challenges. *Physics in Medicine and Biology*, 64(1), 2019.

[46] Leonor Michaelis, Maud Leonora Menten, Kenneth A Johnson, and Roger S Goody. The original michaelis constant: translation of the 1913 michaelis-menten paper. *Biochemistry*, 50(39):8264—8269, October 2011.

[47] Mohammad Moeini, Xuecong Lu, Pramod K. Avti, Rafat Damseh, Samuel Bélanger, Frédéric Picard, David Boas, Ashok Kakkar, and Frédéric Lesage. Compromised microvascular oxygen delivery increases brain tissue vulnerability with age. *Scientific Reports*, 8:8219, 5 2018.

[48] Ugo Del Monte. Does the cell number 10^9 still really fit one gram of tumor tissue? *Cell Cycle*, 8:505–506, 2 2009.

[49] Barbara Muz, Pilar de la Puente, Feda Azab, and Abdel K. Azab. The role of hypoxia in cancer progression, angiogenesis, metastasis, and resistance to therapy. *Hypoxia*, page 83, 12 2015.

[50] L. Possenti, G. Casagrande, S. Di Gregorio, P. Zunino, and M.L. Costantino. Numerical simulations of the microvascular fluid balance with a non-linear model of the lymphatic system. *Microvascular Research*, 122:101–110, 2019.

[51] L. Possenti, S. Di Gregorio, G. Casagrande, M.L. Costantino, T. Rancati, and P. Zunino. A global sensitivity analysis approach applied to a multiscale model of microvascular flow. *Computer Methods in Biomechanics and Biomedical Engineering*, pages 1–10, 2020.

[52] L. Possenti, S. di Gregorio, F.M. Gerosa, G. Raimondi, G. Casagrande, M.L. Costantino, and P. Zunino. A computational model for microcirculation including fahraeus-lindqvist effect, plasma skimming and fluid exchange with the tissue interstitium. *International Journal for Numerical Methods in Biomedical Engineering*, 35(3), 2019.

[53] Luca Possenti, Alessandro Cicchetti, Riccardo Rosati, Daniele Cerroni, Maria Laura Costantino, Tiziana Rancati, and Paolo Zunino. A mesoscale computational model for microvascular oxygen transfer. *Annals of Biomedical Engineering*, 6 2021.

[54] Gibin Powathil, Mohammad Kohandel, Michael Milosevic, and Siv Sivaloganathan. Modeling the spatial distribution of chronic tumor hypoxia: Implications for experimental and clinical studies. *Computational and Mathematical Methods in Medicine*, 2012:1–11, 2012.

[55] A R Pries and T W Secomb. Microvascular blood viscosity in vivo and the endothelial surface layer. *American journal of physiology. Heart and circulatory physiology*, 289(6):H2657–H2664, 2005.

[56] Johanna Ramroth, David J. Cutter, Sarah C. Darby, Geoff S. Higgins, Paul McGale, Mike Partridge, and Carolyn W. Taylor. Dose and fractionation in radiation therapy of curative intent for non-small cell lung cancer: Meta-analysis of randomized trials. *International Journal of Radiation Oncology*Biology*Physics*, 96:736–747, 11 2016.

[57] Y. Renard and K. Poulios. Getfem: Automated fe modeling of multiphysics problems based on a genericweak form language. *ACM Transactions on Mathematical Software*, 47(1), 2021.

[58] Sergio Rey, Luana Schito, Marianne Koritzinsky, and Bradly G. Wouters. Molecular targeting of hypoxia in radiotherapy. *Advanced Drug Delivery Reviews*, 109:45–62, 1 2017.

[59] Bengt Rippe, Akira Kamiya, and Björn Folkow. Simultaneous measurements of capillary diffusion and filtration exchange during shifts in filtration-absorption and at graded alterations in the capillary permeability surface area product (ps). *Acta Physiologica Scandinavica*, 104:318–336, 11 1978.

[60] Sava Sakadžić, Emiri T. Mandeville, Louis Gagnon, Joseph J. Musacchia, Mohammad A. Yaseen, Meryem A. Yucel, Joel Lefebvre, Frédéric Lesage, Anders M. Dale, Katharina Eikermann-Haerter, Cenk Ayata, Vivek J. Srinivasan, Eng H. Lo, Anna Devor, and David A. Boas. Large arteriolar component of oxygen delivery implies a safe margin of oxygen supply to cerebral tissue. *Nature Communications*, 5:5734, 12 2014.

[61] Ahmed Salem. Hypoxia-targeted dose painting in radiotherapy. *Seminars in Radiation Oncology*, 33:298–306, 7 2023.

[62] Filippo Schiavo, Emely Kjellsson Lindblom, and Iuliana Toma-Dasu. Towards the virtual tumor for optimizing radiotherapy treatments of hypoxic tumors: A novel model of heterogeneous tissue vasculature and oxygenation. *Journal of Theoretical Biology*, 547:111175, 8 2022.

[63] Jacob G. Scott, Alexander G. Fletcher, Alexander R. A. Anderson, and Philip K. Maini. Spatial metrics of tumour vascular organisation predict radiation efficacy in a computational model. *PLOS Computational Biology*, 12:e1004712, 1 2016.

[64] T. W. Secomb. Blood flow in the microcircaulation. *Annual Review of Fluid Mechanics*, 49:443–461, 2017.

[65] T.W. SECOMB, R. HSU, N.B. BEAMER, and B.M. COULL. Theoretical simulation of oxygen transport to brain by networks of microvessels: Effects of oxygen supply and demand on tissue hypoxia. *Microcirculation*, 7:237–247, 8 2000.

[66] T.W. Secomb, R. Hsu, E.T. Ong, J.F. Gross, and M.W. Dewhirst. Analysis of the effects of oxygen supply and demand on hypoxic fraction in tumors. *Acta Oncologica*, 34(3):313–316, 1995.

[67] T.W. Secomb, R. Hsu, E.Y.H. Park, and M.W. Dewhirst. Green's function methods for analysis of oxygen delivery to tissue by microvascular networks. *Annals of Biomedical Engineering*, 32(11):1519–1529, 2004.

[68] T.W. Secomb and A.R. Pries. The microcirculation: Physiology at the mesoscale. *Journal of Physiology*, 589(5):1047–1052, 2011.

[69] M. Sefidgar, M. Soltani, K. Raahemifar, M. Sadeghi, H. Bazmara, M. Bazargan, and M. Mousavi Naeenian. Numerical modeling of drug delivery in a dynamic solid tumor microvasculature. *Microvascular Research*, 99:43–56, 2015.

[70] F. Smith A, V. Doyeux, M. Berg, M. Peyrounette, M. Haft-Javaherian, E. Larue A, H. Slater J, F. Lauwers, P. Blinder, P. Tsai, D. Kleinfeld, B. Schaffer C, N. Nishimura, Y. Davit, and S. Lorthois. Brain capillary networks across species: A few simple organizational requirements are sufficient to reproduce both structure and function. *Frontiers in Physiology*, 10, 2019.

[71] L. Strigari, F. Torriani, L. Manganaro, T. Inaniwa, F. Dalmasso, R. Cirio, and A. Attili. Tumour control in ion beam radiotherapy with different ions in the presence of hypoxia: An oxygen enhancement ratio model based on the microdosimetric kinetic model. *Physics in Medicine and Biology*, 63(6), 2018.

[72] Melody A. Swartz and Mark E. Fleury. Interstitial flow and its effects in soft tissues. *Annual Review of Biomedical Engineering*, 9:229–256, 2007.

[73] P.W. Sweeney, A. D'esposito, S. Walker-Samuel, and R.J. Shipley. Modelling the transport of fluid through heterogeneous, whole tumours in silico. *PLoS Computational Biology*, 15(6), 2019.

[74] Walter Tinganelli, Marco Durante, Ryoichi Hirayama, Michael Krämer, Andreas Maier, Wilma Kraft-Weyrather, Yoshiya Furusawa, Thomas Friedrich, and Emanuele Scifoni. Kill-painting of hypoxic tumours in charged particle therapy. *Scientific Reports*, 5:17016, 11 2015.

[75] Iuliana Toma-Dasu and Alexandru Dasu. Modelling tumour oxygenation, reoxygenation and implications on treatment outcome. *Computational and Mathematical Methods in Medicine*, 2013:1–9, 2013.

[76] Iuliana Toma-Dasu and Alexandru Dasu. Towards multidimensional radiotherapy: Key challenges for treatment individualisation. *Computational and Mathematical Methods in Medicine*, 2015:1–8, 2015.

[77] Piermario Vitullo, Ludovica Cicci, Luca Possenti, Alessandro Coclite, Maria Laura Costantino, and Paolo Zunino. Sensitivity analysis of a multi-physics model for the vascular microenvironment. *International Journal for Numerical Methods in Biomedical Engineering*, 7 2023.

[78] M. Welter, T. Fredrich, H. Rinneberg, and H. Rieger. Computational model for tumor oxygenation applied to clinical data on breast tumor hemoglobin concentrations suggests vascular dilatation and compression. *PLoS ONE*, 11(8), 2016.

[79] T. Wenzl and J.J. Wilkens. Modelling of the oxygen enhancement ratio for ion beam radiation therapy. *Physics in Medicine and Biology*, 56(11):3251–3268, 2011.

[80] T. Wenzl and J.J. Wilkens. Theoretical analysis of the dose dependence of the oxygen enhancement ratio and its relevance for clinical applications. *Radiation Oncology*, 6(1), 2011.

[81] Derek A. White, Zhang Zhang, Li Li, Jeni Gerberich, Strahinja Stojadinovic, Peter Peschke, and Ralph P. Mason. Developing oxygen-enhanced magnetic resonance imaging as a prognostic biomarker of radiation response. *Cancer Letters*, 380:69–77, 9 2016.

[82] Michael Yan, Andre G. Gouveia, Fabio L. Cury, Nikitha Moideen, Vanessa F. Bratti, Horacio Patrocinio, Alejandro Berlin, Lucas C. Mendez, and Fabio Y. Moraes. Practical considerations for prostate hypofractionation in the developing world. *Nature Reviews Urology*, 18:669–685, 11 2021.

MOX Technical Reports, last issues

Dipartimento di Matematica
Politecnico di Milano, Via Bonardi 9 - 20133 Milano (Italy)

64/2024 Cavazzutti, M.; Arnone, E.; Ferraccioli, F.; Galimberti, C.; Finos, L.; Sangalli, L.M.
Sign-Flip inference for spatial regression with differential regularization

63/2024 Vitullo, P.; Franco, N.R.; Zunino, P.
Deep learning enhanced cost-aware multi-fidelity uncertainty quantification of a computational model for radiotherapy

62/2024 Roknian, A.A.; Scotti, A.; Fumagalli, A.
Free convection in fractured porous media: a numerical study

59/2024 Carbonaro, D.; Ferro, N.; Mezzadri, F.; Gallo, D.; Audenino, A.; Perotto, S.; Morbiducci, U.; Chiastra, C.
Easy-to-use formulations based on the homogenization theory for vascular stent design and mechanical characterization

60/2024 Temellini, E.; Ferro, N.; Stabile, G.; Delgado Avila, E.; Chacon Rebollo, T.; Perotto, S.
Space - time mesh adaptation for the VMS - Smagorinsky modeling of high Reynolds number flows

61/2024 Speroni, G.; Ferro, N.
A novel metric - based mesh adaptation algorithm for 3D periodic domains

Possenti, L.; Vitullo, P.; Cicchetti, A.; Zunino, P.; Rancati, T.
Modeling Hypoxia-Induced Radiation Resistance and the Impact of Radiation Sources

Roknian, A.A.; Scotti, A.; Fumagalli, A.
Free convection in fractured porous media: a numerical study

Temellini, E.; Ferro, N.; Stabile, G.; Delgado Avila, E.; Chacon Rebollo, T.; Perotto, S.
Space-time mesh adaptation for the VMS-Smagorinsky modeling of high Reynolds number flows

Speroni, G.; Ferro, N.
A novel metric-based mesh adaptation algorithm for 3D periodic domains